

ENHANCING PERFORMANCE OF SOLAR CELLS VIA WAVEFRONT
SHAPING

A THESIS SUBMITTED TO
THE GRADUATE SCHOOL OF NATURAL AND APPLIED SCIENCES
OF
MIDDLE EAST TECHNICAL UNIVERSITY

BY

SENA ATİLA

IN PARTIAL FULFILLMENT OF THE REQUIREMENTS
FOR
THE DEGREE OF MASTER OF SCIENCE
IN
MICRO AND NANOTECHNOLOGY

AUGUST 2022

Approval of the thesis:

**ENHANCING PERFORMANCE OF SOLAR CELLS VIA WAVEFRONT
SHAPING**

submitted by **SENA ATİLA** in partial fulfillment of the requirements for the degree
of **Master of Science in Micro and Nanotechnology Department, Middle East
Technical University** by,

Prof. Dr. Halil Kalıpçılar
Dean, Graduate School of **Natural and Applied Sciences**

Prof. Dr. Deniz Üner
Head of Department, **Micro and Nanotechnology**

Assoc. Prof. Dr. Emre Yüce
Supervisor, **Physics, METU**

Examining Committee Members:

Assoc. Prof. Dr. Mustafa Kulakcı
Department of Physics, Eskişehir Technical University

Assoc. Prof. Dr. Emre Yüce
Department of Physics, METU

Prof. Dr. Bülent Gültekin Akınoğlu
Department of Physics, METU

Prof. Dr. Mehmet Parlak
Department of Physics, METU

Prof. Dr. Ali Çırpan
Department of Chemistry, METU

Date: 25.08.2022

I hereby declare that all information in this document has been obtained and presented in accordance with academic rules and ethical conduct. I also declare that, as required by these rules and conduct, I have fully cited and referenced all material and results that are not original to this work.

Name, Surname: SENA ATİLA

Signature :

ABSTRACT

ENHANCING PERFORMANCE OF SOLAR CELLS VIA WAVEFRONT SHAPING

ATILA, SENA

M.S., Department of Micro and Nanotechnology

Supervisor: Assoc. Prof. Dr. Emre Yüce

August 2022, 63 pages

Solar energy has a great potential to provide for our energy demand. However, due to the broadband nature of the Sun, solar cells encounter efficiency losses. For single-junction GaAs solar cells, the efficiency is measured as 27.6% at most [1]. Previously, the broadband light is experimentally split and concentrated to chosen positions on the CCD camera as three sub-bands to utilize the full spectrum of the Sun, and a particular type of diffractive optical element (SpliCon) is obtained [2].

In this thesis, we demonstrate a system with optical elements, a gallium arsenide (GaAs) solar cell and Si/InGaAs photodetectors for the concentration of the broadband light (360 - 2600 nm) to increase the performance of the solar cell and photodetectors. After passing through several optical elements, broadband light is spatially controlled on laterally arranged GaAs solar cell and Si/InGaAs photodetectors via a spatial light modulator (SLM). By sequentially scanning each pixel of the SLM, we alter the phase of the incident light, and consequently, we increase the electrical current generated by GaAs solar cell. We obtain an excess $\sim 6\%$ to $\sim 11\%$ short-circuit current read from GaAs. At the maximum power point, the excess current varies from

$\sim 10\%$ to $\sim 20\%$, while the power output increases from $\sim 6\%$ to $\sim 14\%$ for the different numbers of superpixels. For Si and InGaAs photodetector, we achieve $\sim 6\%$ to $\sim 13\%$ and $\sim 9\%$ to $\sim 16\%$ RMS voltage value, respectively.

Keywords: wavefront shaping, spatial light modulator, diffractive optical element, solar energy, solar concentration

ÖZ

DALGAÖNÜ ŞEKİLLENDİRME İLE GÜNEŞ HÜCRELERİNİN PERFORMANSINI ARTIRMA

ATİLA, SENA

Yüksek Lisans, Mikro ve Nanoteknoloji Bölümü

Tez Yöneticisi: Doç. Dr. Emre Yüce

Ağustos 2022 , 63 sayfa

Güneş enerjisi, enerji ihtiyacımızı karşılamak için büyük bir potansiyele sahiptir. Ancak Güneş'in geniş bant yapısı nedeniyle, güneş hücreleri verim kayıpları yaşamaktadır. Tek eklemlili GaAs güneş hücresi için ölçülen en yüksek verim 27.6% olarak kaydedilmiştir [1]. Daha önceki çalışmalarda, geniş bant ışık, Güneş'in tam spektrumunu kullanmak amacıyla deneysel olarak üç bant aralığına ayrılmış ve konsantre edilmiştir, ve özel bir kırınım optik eleman (SpliCon) elde edilmiştir [2].

Bu tezde, güneş hücrelerinin ve fotodetektörlerin performansını artırmak için optik elemanlarla, GaAs güneş hücresiyle ve Si/InGaAs fotodetektörlerle ışığı odaklamak için bir sistem tanıtıyoruz. Geniş bant ışık birçok optik elemandan geçtikten sonra, bir uzaysal ışık modülatörü (SLM) aracılığıyla yanal olarak yerleştirilmiş GaAs güneş pili ve Si/InGaAs fotodetektörleri üzerinde uzaysal olarak kontrol edilir. SLM'in her bir pikselini sırayla tarayarak gelen ışığın fazını değiştiririz ve sonuç olarak GaAs güneş hücresinin ürettiği akımı artırırız. GaAs güneş hücresinden okunan kısa devre akımı en az $\sim 6\%$ ve en fazla $\sim 11\%$ artmıştır. Maksimum güç noktasında, okunan akım $\sim 10\%$ değerinden $\sim 20\%$ değerine kadar artış göstermiştir, bu sırada ise farklı

süperpiksel sayıları için güç çıktısı $\sim 6\%$ değerinden $\sim 14\%$ değerine kadar artmıştır. Si ve InGaAs fotodedektörleri için, sırasıyla $\sim 6\%$ değerinden $\sim 13\%$ değerine ve $\sim 9\%$ değerinden $\sim 16\%$ değerine kadar karekök ortalama voltaj değeri artmıştır.

Anahtar Kelimeler: dalgaönü şekillendirme, uzamsal ışık modülatörü, kırınımlı optik element, güneş enerjisi, güneş enerjisi konsantrasyonu

to my future

ACKNOWLEDGMENTS

I would like to express my gratitude towards my supervisor Assoc. Prof. Dr. Emre Yüce for providing guidance through the study. I would like to thank my friends from the Programmable Photonics group for the brainstorming sessions as well as the enjoyable time.

I am extremely thankful to Alp whom I shared many cherished moments, and my dearest friends Buse and Elçin who are always by my side. Finally, I would like to thank my family for their never ending and unconditional support throughout years.

I would like to thank Dr. E. Hande Çiftınar and Prof. Dr. Raşit Turan for their guidance about solar cells, and Assoc. Prof. Dr. Mustafa Kulakçı for providing us GaAs solar cells. I hereby acknowledge the financial support from Tüba Gebip and The Scientific and Technological Research Council of Turkey (TÜBİTAK) under grant number 118F075 and 118E995.

TABLE OF CONTENTS

ABSTRACT	v
ÖZ	vii
ACKNOWLEDGMENTS	x
TABLE OF CONTENTS	xi
LIST OF TABLES	xiv
LIST OF FIGURES	xv
LIST OF ABBREVIATIONS	xx
CHAPTERS	
1 INTRODUCTION	1
1.1 Solar Energy	1
1.1.1 Solar Cells and Utilization of Solar Energy	2
1.1.1.1 Diffractive Optical Elements (DOEs)	5
2 THEORY	7
2.1 Diffraction of the Light	7
2.1.1 Fresnel Diffraction	7
2.1.2 Fraunhofer Diffraction	10
2.1.2.1 Fraunhofer Diffraction Through a Rectangular Aperture	11
2.1.2.2 Fraunhofer Diffraction Through a Circular Aperture . .	11

2.1.3	The Fresnel Zone Plate	13
2.1.4	Diffraction Gratings	15
2.1.5	Diffraction Optical Elements (DOEs) and SpliCon	18
3	INSTRUMENTATION AND METHODS	23
3.1	The Experimental Setup	23
3.1.1	Noise Measurement of the Light Source	24
3.1.2	Spatial Light Modulator (SLM)	25
3.1.3	Characteristics of the GaAs Solar Cell	27
3.2	Sourcemeter Connection	31
3.3	The Optimization Algorithm	36
4	RESULTS AND DISCUSSION	37
4.1	Spectral Splitting and Concentration of the Broadband Light on the CCD Camera	37
4.2	Enhancing Performance of the GaAs Solar Cell via Wavefront Shaping	40
4.2.1	Reference and Noise Measurements of GaAs	40
4.2.2	Achieving Excess Current via Concentration on GaAs	42
4.3	Optimization of Si Solar Cell via Wavefront Shaping	49
4.3.1	Reference and Noise Measurements of Si	49
4.4	Enhancing Performance of the Silicon Photodetector	51
4.4.1	Noise Measurement of the Si Photodetector	51
4.4.2	Achieving Excess Current via Concentration on the Si Pho- todetector	51
4.5	Enhancing Performance of the InGaAs Photodetector	52
4.5.1	Noise Measurement of the InGaAs Photodetector	54

4.5.2	Achieving Excess Current via Concentration on the InGaAs Photodetector	54
5	CONCLUSION	57
	REFERENCES	59

LIST OF TABLES

TABLES

Table 4.1	The calculated excess short circuit current of GaAs solar cell for five different number of superpixels.	43
Table 4.2	The calculated excess current of GaAs solar cell at the maximum power point for five different number of superpixels.	46
Table 4.3	The calculated excess power of GaAs solar cell at the maximum power point for five different number of superpixels.	46
Table 4.4	The calculated excess RMS value of silicon photodetector for five different number of superpixels.	52
Table 4.5	The calculated excess RMS value of InGaAs photodetector for five different number of superpixels.	54

LIST OF FIGURES

FIGURES

- Figure 1.1 The solar spectrum from 250 nm to 2500 nm inside the atmosphere of the Earth. The ripples are caused by the medium of the atmosphere such as dust particles, water vapor and gas molecules. This figure is taken from [3]. 2
- Figure 1.2 Full solar spectrum and the spectra of silicon solar cell are shown. This figure is directly taken from [4]. 3
- Figure 2.1 A light wave with an amplitude of $U(x,y)$ passing through an aperture forms a wave with a complex amplitude of $f(x,y)$. After a distance L in the free space, a wave with a complex amplitude $g(x,y)$ is observed at the observation plane. The figure is adapted from [5]. 8
- Figure 2.2 Fraunhofer diffraction pattern through a rectangular aperture where D_x and D_y are the dimensions of the aperture and L is the distance between aperture plane and observation plane. The figure is adapted from [5]. 12
- Figure 2.3 Fraunhofer diffraction pattern through a circular aperture where D is the diameter of the aperture, L is the distance between aperture plane and observation plane, and $\rho_s = \frac{1.22\lambda L}{D}$. The figure is adapted from [5]. 13
- Figure 2.4 (a) Positive Zone plate with even number of opaque zones and odd number of transparent zones and (b) negative Zone plate with odd number of opaque zones and even number of transparent zones. 14

Figure 2.5	A source at the point S is placed in a distance r away from the central point of the Zone plate. The distance between central point and focal point F is f , and the optical path between source and focal point is denoted as h . The figure is adapted from [6].	15
Figure 2.6	(a) Reflection type of diffractive optical element where the incident light and the diffracted light are on the same side and (b) transmission type of diffractive optical element where the incident light and the diffracted light are on the opposite side. The figure is adapted from [7]. .	16
Figure 2.7	Diffraction grating with illuminated by two parallel rays denoted as 'Ray 1' and 'Ray 2'. Both rays are in phase at the wavefronts A and B. The figure is adapted from [7].	17
Figure 2.8	A DOE with varying discrete height values can be represented as the difference between two phase structures. The figure is adapted from [8].	20
Figure 2.9	(a) A DOE with seven varying height values, and (b) the surface of the SLM with seven varying refractive indices. While both DOE and SLM have the same dimension along the x and y directions, the height value of DOE changes along the z direction.	21
Figure 3.1	The experimental setup to concentrate broadband light on GaAs solar cell and Si/InGaAs photodetectors. A fiber-coupled broadband light goes through a condenser lens with a focal length of 160 mm and a polarizer, and two mirrors. After, the light is reflected to the GaAs and silicon photodetector by a lens with a focal length of 300 mm through the SLM surface. The measurements are obtained through Keithley sourcemeter for GaAs solar cell, and collected by an oscilloscope for photodetectors.	24
Figure 3.2	A schematic representation of layers of the SLM where each LC material is attached to an electrode. The figure is adapted from [9]. . . .	26

Figure 3.3	LC materials aligned parallel to the both substrates without voltage, and a tilted direction of alignment of LC material with an applied voltage resulting in a phase modulation, respectively.	27
Figure 3.4	Fabricated GaAs solar cell via molecular beam epitaxy where the doping and material types are shown.	28
Figure 3.5	Typical IV curve of a solar cell. Solar cell characteristics are denoted on the graph which are short circuit current, open circuit voltage and maximum power point (MPP).	29
Figure 3.6	(a) Transmittance spectrum and (b) absorbance spectrum of GaAs solar cell with respect to wavelength in between 300 nm and 1000 nm. .	30
Figure 3.7	External quantum efficiency of GaAs solar cell with respect to wavelength in between 440 nm and 1100 nm.	31
Figure 3.8	The circuit which represents 2-wire measurement.	32
Figure 3.9	The circuit which represents 4-wire measurement where the resistance of wires that are attached to the voltmeter are in the order of picoamperes, thus they are negligible.	33
Figure 3.10	Representation of Kelvin probes which are attached to a sourcemeter connection. "C" represents the wire where the test current is forced, while "P" represents the potential where the measurement is carried out. The cables of Kelvin probes are insulated from each other, and may only contact to each other on the terminals of the subject.	33
Figure 3.11	(a) The schematic representation of Keithley 2440 model. (b) The platform for solar cell measurement including GaAs solar cell that is placed on a copper plate, and Kelvin probes connected to Keithley 2440 on the left side and contacted to the terminals of GaAs on the right side. Copper plate where the GaAs solar cell is attached behaves as negative of the solar cell. The black box shown in (a) is attached to the copper plate, and the red box shown in (a) is attached to anode of the GaAs solar cell.	35

Figure 4.1	The CCD image (a) before the optimization of the SLM surface, (b) after the optimization of the SLM surface to concentrate light on the desired positions and (c) resulting phase pattern on the SLM surface to split and concentrate the broadband light on desired positions. Red channel is concentrated from $(x,y) = (1.11 \text{ mm}, 1.7 \text{ mm})$ to $(x,y) = (1.48 \text{ mm}, 2.1 \text{ mm})$, and green and blue channels are concentrated from $(x,y) = (3.34 \text{ mm}, 1.7 \text{ mm})$ to $(x,y) = (3.71 \text{ mm}, 2.1 \text{ mm})$	38
Figure 4.2	Varying (a) enhancement factors and (b) spectral splitting ratios according to the different number of superpixels for the red channel, the green channel and the blue channel.	39
Figure 4.3	The reference (a) dark current density (b) two photocurrent current density measurements for GaAs which are taken under 1 sun illumination.	40
Figure 4.4	The reference (a) dark current density (b) two photocurrent current density measurements for GaAs which are taken under 1 sun illumination, converted to the first quadrant for convenience.	41
Figure 4.5	The semi-log IV curve of GaAs where the current measured at reverse bias is steady. The optimization bias is chosen as -0.2 V where the noise is 0.5%.	41
Figure 4.6	GaAs noise measurement is calculated according to the equation 43. It is obvious that the noise is below 1% at the most of reverse bias region.	42
Figure 4.7	SLM phase pattern for GaAs optimized with (a) 829 superpixels (b) 1296 superpixels (c) 2304 superpixels (d) 5184 superpixels (e) 20736 superpixels. The shape of GaAs solar cell is clearly observed on the SLM phase pattern.	44
Figure 4.8	Excess current (%) values are plotted with (a) the dark current (calculated via equation 44) and (b) without the dark current (calculated via equation 45).	45

Figure 4.9	The current density vs voltage curve of GaAs solar cell which are taken for the dark current, the photocurrent and current measured for five different number of superpixels. Rise of the short circuit current and the open circuit voltage is clearly seen on the graph.	45
Figure 4.10	The power density vs voltage curve of GaAs solar cell which are taken for the photocurrent and current measured with different number of superpixels. The maximum power point (MPP) shifts to 115 mV from 110 mV for each number of superpixels, and the power density values also increase.	47
Figure 4.11	Calculated excess current for different positions. The current for blue curve is for when GaAs is placed 43 cm after SLM. The current for red curve is for when GaAs is placed 42 cm after SLM. The current for yellow curve is for when GaAs is placed 41 cm after SLM.	48
Figure 4.12	(a) The reference current for dark current and photocurrent of Si, and (b) the converted data to the first quadrant for convenience. . . .	49
Figure 4.13	Si noise measurement is calculated according to the equation 43. The noise is below 10% until 2.4 mV bias.	50
Figure 4.14	The optimized SLM phase pattern for Si solar cell by using the same algorithm for optimization of GaAs solar cell. It is evident that there is no concentration on the solar cell.	50
Figure 4.15	SLM phase pattern for silicon photodetector optimized with (a) 829 superpixels (b) 1296 superpixels (c) 2304 superpixels (d) 5184 superpixels (e) 20736 superpixels. The shape of silicon photodetector is clearly observed on the SLM phase pattern.	53
Figure 4.16	SLM phase pattern for InGaAs photodetector optimized with (a) 829 superpixels (b) 1296 superpixels (c) 2304 superpixels (d) 5184 superpixels (e) 20736 superpixels. The shape of InGaAs photodetector is clearly seen on the SLM phase pattern.	55

LIST OF ABBREVIATIONS

AM	Air Mass
DOE	Diffractive Optical Element
GaAs	Gallium Arsenide
IR	Infrared
LC	Liquid Crystal
MPP	Maximum Power Point
RMS	Root Mean Square
Si	Silicon
SLM	Spatial Light Modulator
SpliCon	Spectral Splitter and Solar Concentrator
UV	Ultraviolet

CHAPTER 1

INTRODUCTION

1.1 Solar Energy

The solar spectrum covers the light emission from gamma waves to radio waves. Nevertheless, the radiation of the sun gives a peak at visible wavelengths. The irradiance is defined as Joules per second per m^2 of the illuminated area per nm of the wavelength. As a result, the unit of irradiance becomes $\text{W}/\text{m}^2/\text{nm}$, and a typical irradiance of the solar spectrum is plotted with respect to the wavelength as shown in Fig. 1.1. The figure shows the blackbody radiation of the Sun. The blackbody radiation of the Sun is not a perfect curve, and has ripples. The ripples in Fig. 1.1 are caused by absorption of components that exist on the atmosphere of the Earth such as dust particles, water vapor (H_2O) and gas molecules like carbon dioxide (CO_2) in the IR region, and ozone (O_3) and oxygen (O_2) in the UV region [10, 11, 12].

The Sun radiates a spectrum at approximately 5743 °K for AM0 [13]. AM denotes the phrase 'air mass'. The air mass coefficient in the equation 11 is described as the ratio of the path length of the light through the atmosphere at a direct angle to the path length of the light through the atmosphere at a specific angle (α). AM0 is the spectrum outside of the Earth's atmosphere, while AM1 and AM1.5 express the spectrum inside the Earth's atmosphere with direct illumination and angled (48°) illumination, respectively.

$$\text{Air Mass (AM) Coefficient} = \frac{1}{\cos\alpha} \quad (11)$$

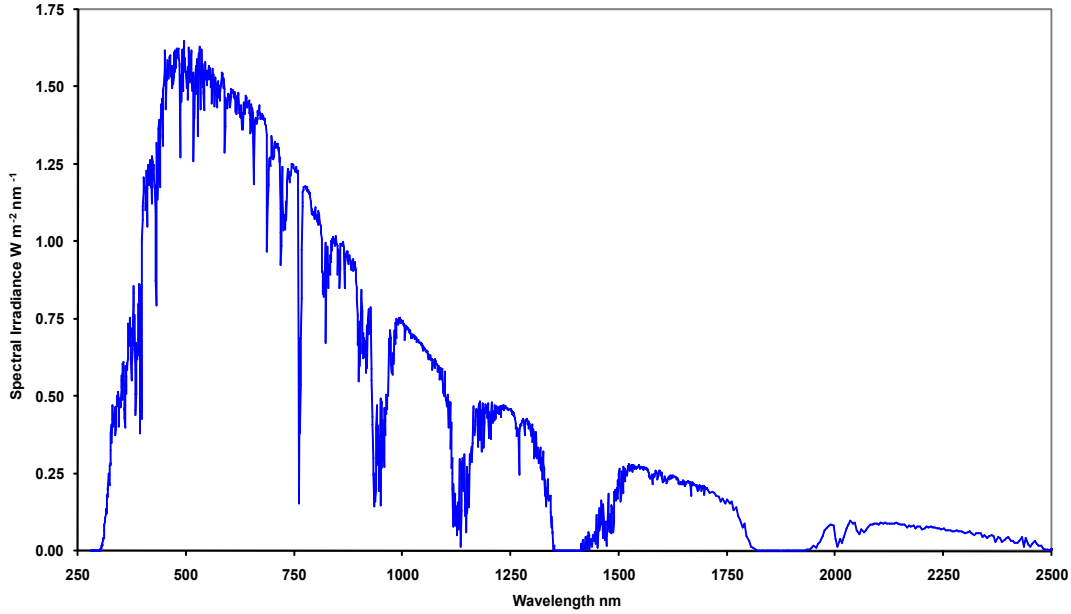


Figure 1.1: The solar spectrum from 250 nm to 2500 nm inside the atmosphere of the Earth. The ripples are caused by the medium of the atmosphere such as dust particles, water vapor and gas molecules. This figure is taken from [3].

1.1.1 Solar Cells and Utilization of Solar Energy

Single junction solar cells are the most commonly used photovoltaic devices of the moment. However, single junction solar cells suffer from an efficiency loss due to non-absorption and thermalization, because the full solar spectrum cannot be utilized by the cell due to its limited bandgap energy. The theoretical maximum efficiency that can be reached is $\sim 30\%$ for a solar cell with bandgap energy of 1.1 eV [14]. For GaAs solar cell, the measured efficiency of a single solar cell is recorded as $\sim 27.6\%$ [1, 15]. Non-absorption happens when a photon with a lower energy level than the bandgap energy of the material of the solar cell illuminates the cell, while thermalization occurs when a photon with a higher energy level than bandgap energy illuminated the solar cell, and the cell loses the excess energy via heat. There are several approaches to overcome this limit such as multi-junction solar cells with different bandgap energies [16, 17], spectral splitting methods with prisms [18] and dichroic filters [19, 20], and DOEs to split and concentrate the broadband spectrum [21, 22, 23, 24, 25].

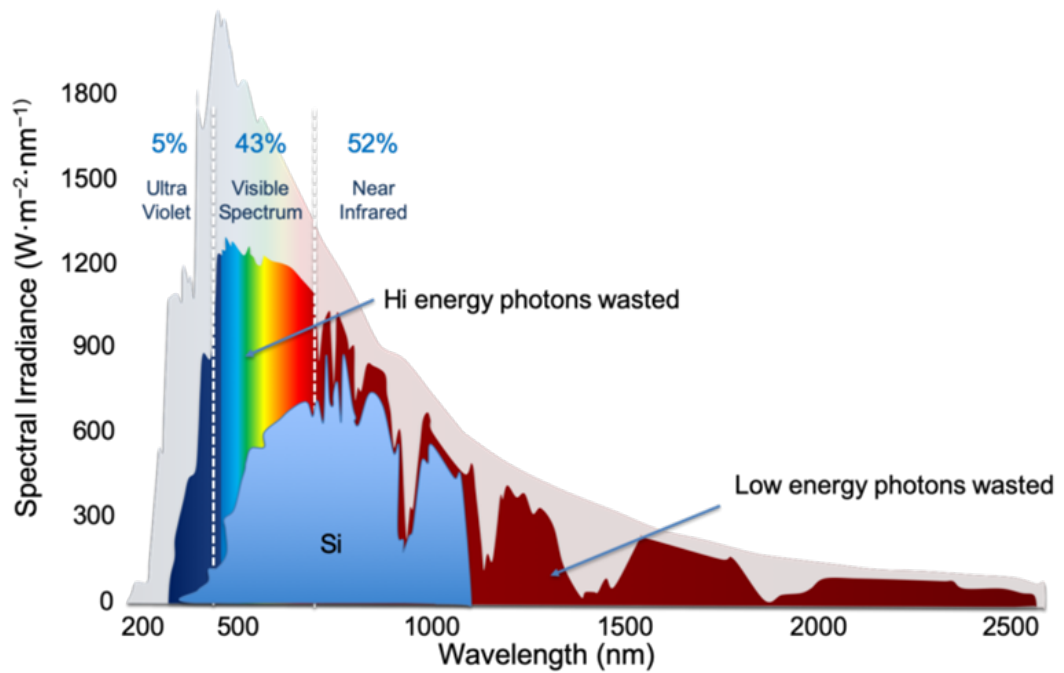


Figure 1.2: Full solar spectrum and the spectra of silicon solar cell are shown. This figure is directly taken from [4].

Multi-junction solar cells, which are also commonly called cascade/tandem solar cells, split in half as vertical multi-junction solar cells and lateral multi-junction solar cells. Vertical multi-junction solar cells involve a series of semiconductor materials connected from higher bandgap energy to lower bandgap energy from top to bottom, respectively. The fundamental advantage of vertical multi-junction solar cells is spectral splitting. While higher energy photons are absorbed in the top semiconductor material, the wasted lower energy photons are absorbed in the bottom semiconductor material. On the other hand, the main disadvantage of vertical multi-junction solar cells is the complexity of fabrication, since there is a restricted choice of materials due to the need for current and lattice matching, resulting in high fabrication costs [22]. Current matching means that an equal current must flow through the serially connected cells, while lattice matching means that the morphology of the materials should be matched [18]. Lateral multi-junction solar cells are basically individual solar cells that are placed laterally to absorb relevant parts of the full spectrum of the light with the help of a spectral splitting element. Since the cells are not stacked

together in lateral multi-junction solar cells, there is no need for current and lattice matching requirements. Therefore, a wider range of materials with better performance as compared to materials used in vertical multi-junction solar cells can be taken into consideration. Additionally, the complexity of the fabrication steps is eliminated, and the fabrication cost drops. Lateral multi-junction solar cells should be combined with a spectral splitting element, otherwise, they do not have a spectral splitting feature on their own like vertical multi-junction solar cells.

Prisms are one of the elements utilized for spectral splitting purposes with laterally placed multi-junction solar cells so that there is no need for current and lattice matching requirements, and the cost of the solar cell decreases. More than that, the system is so plain that the prism can be merged with thin film technologies, where the solar cell is deposited on the prism [18]. Furthermore, the light trapping inside the prism is possible via total internal reflection and with the help of a mirror so that the light is first guided to the high bandgap solar cell, and then reflected towards the low bandgap solar cell. With this configuration, spectral splitting is achieved which is similar to the vertically stacked multi-junction solar cells. However, there is one disadvantage of this configuration. The high bandgap solar cell delivers more power while the low bandgap solar cell delivers less power due to suffering from voltage drop because of poor illumination concentration conditions.

Dichroic filters are another elements that use thin film interference for spectral splitting purposes. Unlike prisms, dichroic filters reflect one spectral band, and transmit the other spectral band to a different position. A basic configuration consists of a dichroic filter which is positioned at a 45° and two solar cells where one solar cell is receiving the reflected light while the other solar cell is receiving the transmitted light. Generally, dichroic filters are placed at a 45° to the incident light, because the transmitted light passes through the filter, and the other part is reflected at a 90° with this placement. There are some losses involved in dichroic filter such as the reflectance of the filter decreases the efficiency in the measurements [20].

1.1.1.1 Diffractive Optical Elements (DOEs)

The light is manipulated via refraction, interference, and/or diffraction spatially and spectrally. Elements of prisms and dichroic mirrors can be included to achieve control over the light. Prisms control the light by utilizing the refraction characteristic, while splitting the incoming beam into various spectral bands. However, due to the weight and area they would require, and the control over the size and position of spectral bands not being precise, prisms are not preferred widely. Dichroic mirrors control the light via interference. In a similar manner to prisms, their volume restricts their usage on a large scale, and they have poor control over the size and position of spectral bands.

Diffractive optical elements (DOEs) allow concentration and splitting of the light effectively where the position and size of the spectral band are controlled by the design parameters of the DOE which we call a SpliCon. They are low-cost, compact and have straightforward fabrication steps which include fabrication as reflective or transmission type of DOE. DOEs can be designed with Gerchberg-Saxton [26] and Yang-Gu algorithms [27], direct binary search [28], genetic local search optimization algorithm [29], rigorous coupled wave analysis [30] and iterative Fourier transform algorithm [31, 32].

DOEs are also utilized in many areas such as improving the efficiency of solar cells [16, 21, 22, 23, 24, 25], beam shaping [33, 34], infrared systems [35], spatial and spectral control of the light via neural networks [36] and laser systems [37]. Specifically in laser systems, a single layer DOE is more relevant due to the diffraction efficiency of a single layer DOE being 100% at a single wavelength. When the wavelength diverges from the design wavelength, the diffraction efficiency of a single layer DOE drops.

CHAPTER 2

THEORY

2.1 Diffraction of the Light

Diffraction of the light takes effect when the light passes through an aperture or the light faces an obstacle resulting in the light waves bending around the obstacle. The intensity of the traveling light can be observed at a distance from the aperture plane which is called the diffraction pattern caused by destructive and constructive interference. The diffraction pattern is not remarkably evident if the aperture is large, which is the case where refraction dictates the pattern. On the contrary, the light shows a wave-like pattern when the dimension of the aperture is small which is in the approximate size of the wavelength of the light or smaller sizes.

In the Fig. 2.1, the wave $U(x,y)$ is transferred through an aperture, resulting in a wave of $f(x,y) = U(x,y)p(x,y)$ where $p(x,y)$ is the aperture function. The aperture function is 1 inside the aperture and 0 outside the aperture. The output wave is denoted as $g(x,y)$ at the observation plane, and the diffraction pattern is $I(x,y) = |g(x,y)|^2$. Calculation of the diffraction pattern can be approximated by two forms which are Fresnel approximation and Fraunhofer approximation.

2.1.1 Fresnel Diffraction

The propagating optical wave with a wavelength of λ has a complex amplitude of $U(x,y,0)$ in the plane $z = 0$, and complex amplitude of $U(x,y,L)$ in the plane $z = L$. The amplitude at $z = 0$ plane, which is the aperture plane, is $f(x,y)$, and the amplitude at $z = L$, which is the observation plane, is $g(x,y)$. The plane wave is $U(x,y,z) = A \exp[-$

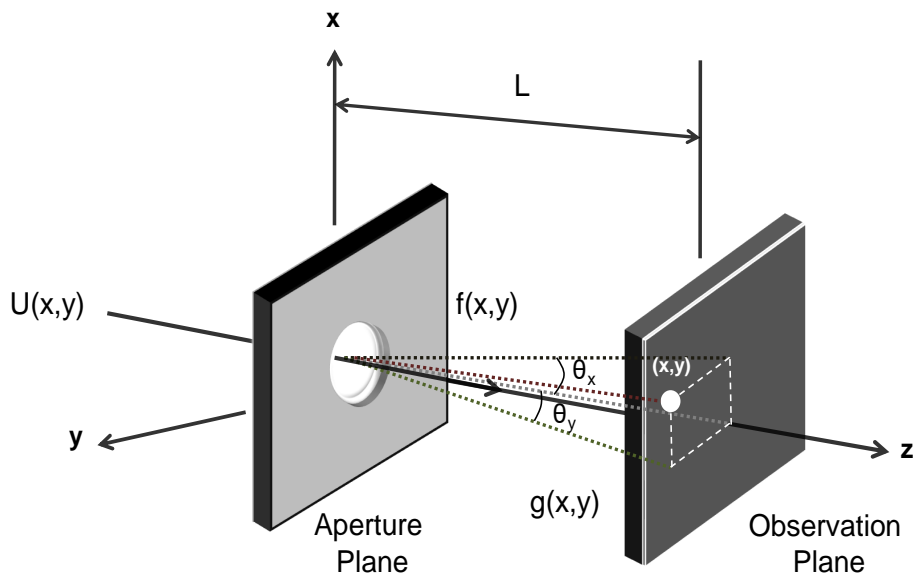


Figure 2.1: A light wave with an amplitude of $U(x,y)$ passing through an aperture forms a wave with a complex amplitude of $f(x,y)$. After a distance L in the free space, a wave with a complex amplitude $g(x,y)$ is observed at the observation plane. The figure is adapted from [5].

$j(k_x x + k_y y + k_z z)$ which becomes a harmonic wave of $f(x, y) = A \exp[-j2\pi(\nu_x x + \nu_y y)]$ where $k_x = 2\pi\nu_x$, $k_y = 2\pi\nu_y$ and $k_z = (k^2 - k_x^2 - k_y^2)^{1/2} = 2\pi(\frac{1}{\lambda^2} - \nu_x^2 - \nu_y^2)^{1/2}$. The wave at observation plane becomes $g(x, y) = A \exp[-j(k_x x + k_y y + k_z L)]$. The transfer function of the free space is the equation 21.

$$H(\nu_x, \nu_y) = \frac{g(x, y)}{f(x, y)} = \exp(-jk_z L) = \exp \left[-j2\pi \left(\frac{1}{\lambda^2} - \nu_x^2 - \nu_y^2 \right)^{1/2} L \right] \quad (21)$$

When the cut off frequency is much larger than spatial frequencies in the complex amplitude of $f(x, y)$, $\nu_x^2 + \nu_y^2 \ll \frac{1}{\lambda^2}$, the transfer function can be simplified into the equation 23 through neglecting the higher terms in the equation 22 where $H_0 = \exp(-jkL)$. In the equation 22, θ is the angle with optical axis and $\theta^2 = \theta_x^2 + \theta_y^2 \simeq \lambda^2 (\nu_x^2 + \nu_y^2)$.

$$2\pi \left(\frac{1}{\lambda^2} - \nu_x^2 - \nu_y^2 \right)^{1/2} L = 2\pi \frac{L}{\lambda} (1 - \theta^2)^{1/2} = 2\pi \frac{L}{\lambda} \left(1 - \frac{\theta^2}{2} + \frac{\theta^4}{8} - \dots \right) \quad (22)$$

$$H(\nu_x, \nu_y) \cong H_0 \exp [j\pi \lambda L (\nu_x^2 + \nu_y^2)] \quad (23)$$

The applicability of Fresnel approximation depends on the largest angle $\theta_m \simeq \frac{r}{L}$, where r is the largest radial distance in the observation plane. Therefore, the condition for Fresnel approximation becomes 24.

$$\frac{N_F \theta_m^2}{4} \ll 1 \quad (24)$$

Let the Fourier transform of the incident wave at aperture plane be the equation 25.

$$F(\nu_x, \nu_y) = \iint_{-\infty}^{\infty} f(x, y) \exp [j2\pi(\nu_x x + \nu_y y)] dx dy \quad (25)$$

The wave at the observation plane is given by $H(\nu_x, \nu_y)F(\nu_x, \nu_y)$ as the equation 26.

$$g(x, y) = H_0 \iint_{-\infty}^{\infty} F(\nu_x, \nu_y) \exp [j\pi \lambda L (\nu_x^2 + \nu_y^2)] \exp [-j2\pi(\nu_x x + \nu_y y)] d\nu_x d\nu_y \quad (26)$$

Let $h(x, y) = h_0 \exp(-jk \frac{x^2 + y^2}{2L})$ be the inverse Fourier transform of the transfer function of the free space where $h_0 = \frac{j}{\lambda L} \exp(-jkL)$, and $f(x', y')$ be the amplitude of a wave that is sent from the point (x', y') . As a result, $f(x', y')h(x - x', y - y')$ becomes the wave created at the observation plane which is the equation 27, and by Fresnel approximation

becomes the equation 28.

$$g(x,y) = h_0 \iint_{-\infty}^{\infty} f(x',y') h(x-x',y-y') dx' dy' \quad (27)$$

$$g(x,y) = h_0 \iint_{-\infty}^{\infty} f(x',y') \exp \left[-j\pi \frac{(x-x')^2 + (y-y')^2}{\lambda L} \right] dx' dy' \quad (28)$$

The complex amplitude of incident wave after aperture is $f(x,y) = I^{1/2} p(x,y)$. Therefore, the intensity of the diffraction pattern becomes the equation 29.

$$I(x,y) = \frac{I}{(\lambda L)^2} \left| \iint_{-\infty}^{\infty} p(x',y') \exp \left[-j\pi \frac{(x-x')^2 + (y-y')^2}{\lambda L} \right] dx' dy' \right|^2 \quad (29)$$

2.1.2 Fraunhofer Diffraction

In the Fig. 2.1, only the plane waves coming at the angles θ_x and θ_y contribute to the complex amplitude of the wave $g(x,y)$ at the point (x,y) , where $\theta_x \approx \frac{x}{L}$ and $\theta_y \approx \frac{y}{L}$. Take the phase value of the equation 26 as the exponential which gives the equation 210.

$$\frac{\pi}{\lambda L} ((x-x')^2 + (y-y')^2) = \frac{\pi}{\lambda L} ((x^2 + y^2) + (x'^2 + y'^2) - 2(xx' + yy')) \quad (210)$$

Fraunhofer approximation, which is also called far-field approximation, is exerted for determination of the light propagation in the sufficiently long distances between the aperture plane and the observation plane, and the aperture radius is small which ensures the equation 211 [5].

$$N_F = \frac{r^2}{\lambda L} \ll 1 \quad (211)$$

The equation denotes Fresnel number, and r is largest radial distance enclosed by the aperture, λ is the wavelength of light and L is the distance between aperture plane and observation plane. As a result, the factor $\frac{\pi}{\lambda L} (x'^2 + y'^2)$ becomes negligible, and the resulting wave is approximated as the equation 212.

$$g(x,y) = h_0 \exp \left[-j\pi \frac{x^2 + y^2}{\lambda L} \right] \iint_{-\infty}^{\infty} f(x',y') \exp \left[j2\pi \frac{xx' + yy'}{\lambda L} \right] dx' dy' \quad (212)$$

Let the frequencies be $\nu_x = \frac{x}{\lambda L}$ and $\nu_y = \frac{y}{\lambda L}$, and the Fourier transform of $f(x,y)$ be $F(\nu_x, \nu_y)$. Therefore, the wave at observation plane becomes the equation 213.

$$g(x,y) = h_0 \exp \left[-j\pi \frac{x^2 + y^2}{\lambda L} \right] F\left(\frac{x}{\lambda L}, \frac{y}{\lambda L}\right) \quad (213)$$

Consider the intensity of incident wave is I which makes $U(x,y)=I^{1/2}$, and $f(x,y)=I^{1/2}p(x,y)$. The wave at observation plane is the equation 215 where $P(\frac{x}{\lambda L}, \frac{y}{\lambda L}) = P(\nu_x, \nu_y)$ is the Fourier transform of $p(x,y)$, and $h_0 = \frac{j}{\lambda L} \exp(-jkL)$.

$$g(x,y) = I^{1/2} h_0 \iint_{-\infty}^{\infty} p(x,y) \exp [j2\pi(\nu_x x + \nu_y y)] dx' dy' \quad (214)$$

$$g(x,y) = I^{1/2} h_0 P\left(\frac{x}{\lambda L}, \frac{y}{\lambda L}\right) \quad (215)$$

The diffraction pattern at the observation plane becomes the equation 216.

$$I(x,y) = \frac{I}{(\lambda L)^2} \left| P\left(\frac{x}{\lambda L}, \frac{y}{\lambda L}\right) \right|^2 \quad (216)$$

2.1.2.1 Fraunhofer Diffraction Through a Rectangular Aperture

The intensity of the diffraction pattern through a rectangular aperture is the equation 217, where D_x and D_y are the dimensions of the aperture, L is the distance between aperture plane and observation plane, and $I_0 = \left(\frac{D_x D_y}{\lambda L}\right)^2 I$ is the peak intensity.

$$I(x,y) = I_0 \text{sinc}^2 \frac{D_x x}{\lambda L} \text{sinc}^2 \frac{D_y y}{\lambda L} \quad (217)$$

2.1.2.2 Fraunhofer Diffraction Through a Circular Aperture

The intensity of the diffraction pattern through a circular aperture is the equation 218, where D is the diameter of the aperture, L is the distance between aperture plane and observation plane, J_1 is the Bessel function in the order of 1, and $I_0 = \left(\frac{\pi D}{4\lambda L}\right)^2 I$ is the peak intensity.

$$I(x,y) = I_0 \left[\frac{2J_1 \left(\frac{\pi D \rho}{\lambda L} \right)}{\frac{\pi D \rho}{\lambda L}} \right]^2, \rho = (x^2 + y^2)^{1/2} \quad (218)$$

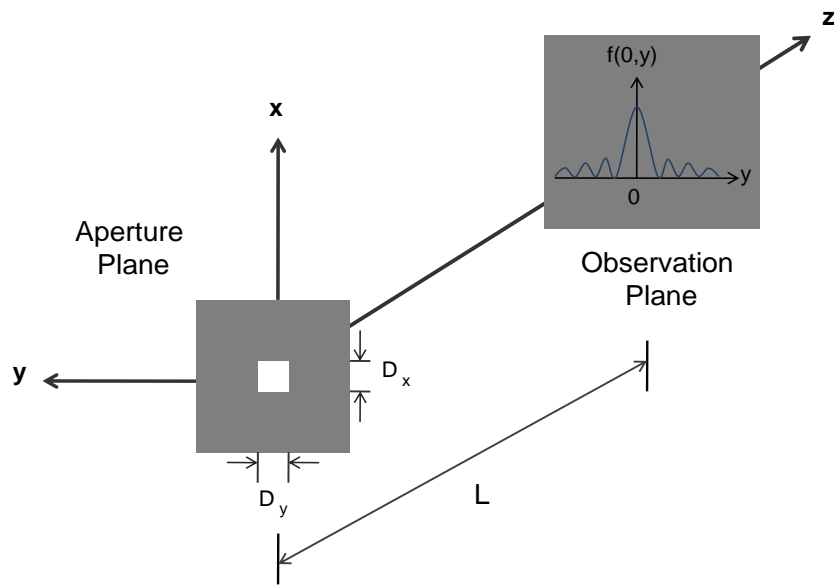


Figure 2.2: Fraunhofer diffraction pattern through a rectangular aperture where D_x and D_y are the dimensions of the aperture and L is the distance between aperture plane and observation plane. The figure is adapted from [5].

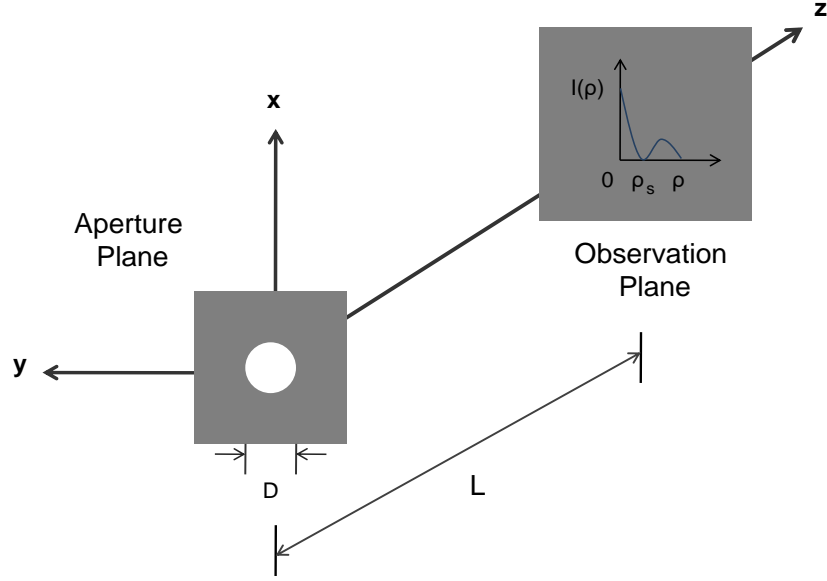


Figure 2.3: Fraunhofer diffraction pattern through a circular aperture where D is the diameter of the aperture, L is the distance between aperture plane and observation plane, and $\rho_s = \frac{1.22\lambda L}{D}$. The figure is adapted from [5].

2.1.3 The Fresnel Zone Plate

The Fresnel Zone is a structure with multiple focal lengths and with interbedded rings which switch between transparency and opacity. If the central zone is transparent, the plate is called a positive Zone plate, while if the central zone is opaque, it is called a negative Zone plate as seen in the Fig. 2.4. Contrary to lenses, zone plates use diffraction to focus the light instead of refraction. The plates are placed in a way that the light passing through transparent plates constructively interfere at the focal point. Assume that we have a source at point S placed to a distance of r away from the center like in Fig. 2.5. The distance between source and focal point is given as $h = \sqrt{(r^2 + f^2)}$. The condition $h - h_0 < \frac{\lambda}{2}$ satisfies constructive interference in the central zone where h_0 is the path length from the source to the focal point, and simply is equal to f in

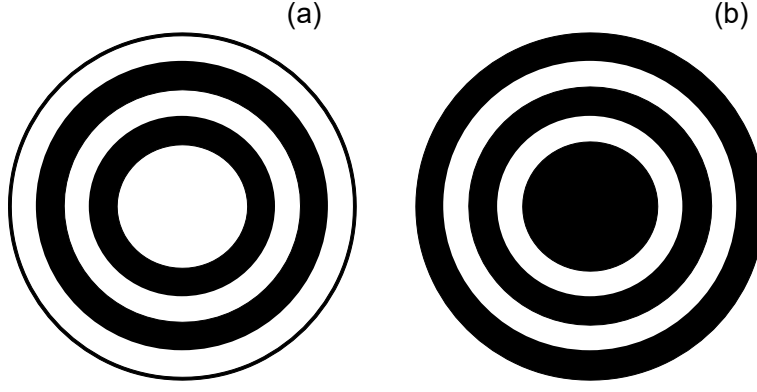


Figure 2.4: (a) Positive Zone plate with even number of opaque zones and odd number of transparent zones and (b) negative Zone plate with odd number of opaque zones and even number of transparent zones.

the Fig. 2.5. When the source enter the second zone, the condition becomes $\frac{\lambda}{2} < h - h_0 < \lambda$ which gives destructive interference. Therefore, the condition for n^{th} zone is found via the equation 219 where n is an integer from 1 to N which denotes the total number of Zone plates. Constructive interference occurs at an odd number of n , while destructive interference occurs at an even number of n .

$$\frac{(n-1)\lambda}{2} < h - h_0 < \frac{n\lambda}{2} \quad (219)$$

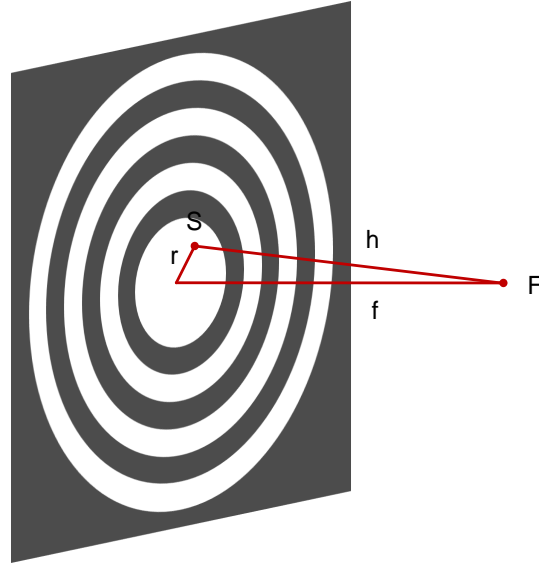


Figure 2.5: A source at the point S is placed in a distance r away from the central point of the Zone plate. The distance between central point and focal point F is f , and the optical path between source and focal point is denoted as h . The figure is adapted from [6].

2.1.4 Diffraction Gratings

When a monochromatic beam with a wavelength of λ hits on a diffraction grating, the light is diffracted towards discrete paths. Each triangle of the grating in Fig. 2.6 is called a groove, and it can be assumed that each groove behaves like a source of diffracted light. When a diffraction grating has a specific discrete angle depending on the spacing of grooves, d , the diffracted light creates constructive interference. In the Fig. 2.6, the light with wavelength of λ is incident on the grating with an angle α , and diffracted at angles β_m . The sign of angle of the diffracted light depends on the side of the incident light.

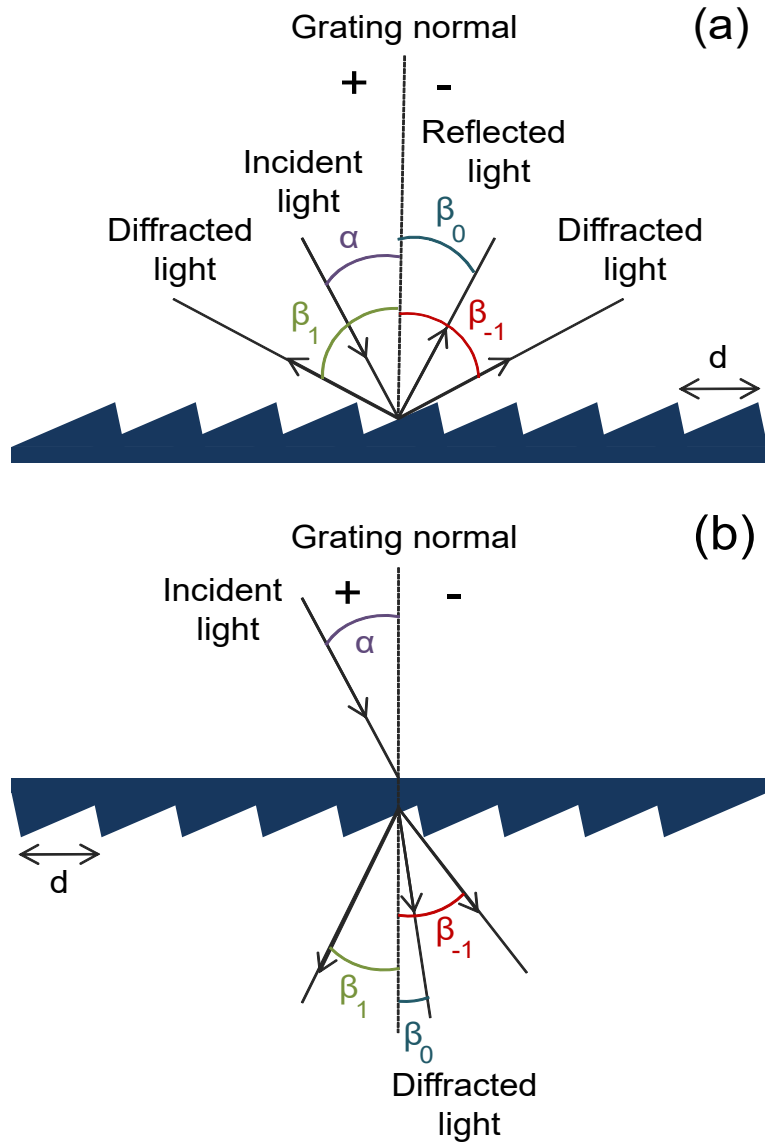


Figure 2.6: (a) Reflection type of diffractive optical element where the incident light and the diffracted light are on the same side and (b) transmission type of diffractive optical element where the incident light and the diffracted light are on the opposite side. The figure is adapted from [7].

In Fig. 2.6, the sign of angles is decided according to the counterclockwise direction from the grating normal. Thus, the angles α and β_1 are positive while the angles β_{-1} and β_0 are negative. For both reflective type and transmission type of diffraction gratings, $\beta_0 = -\alpha$.

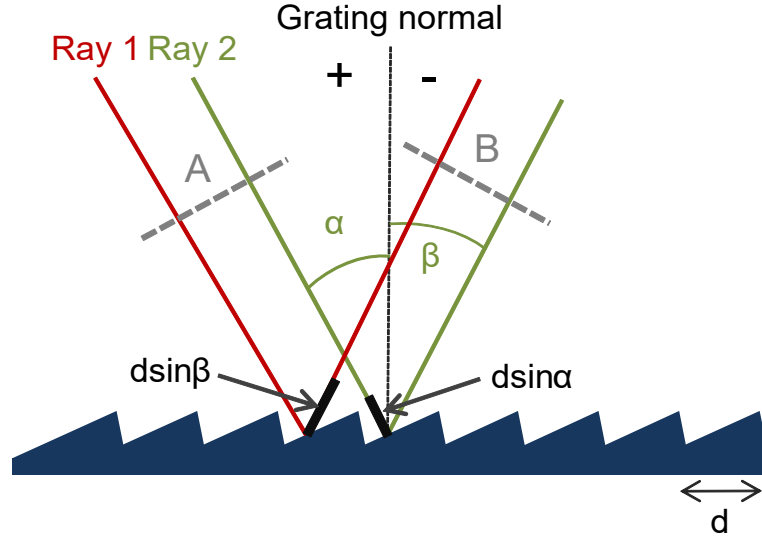


Figure 2.7: Diffraction grating with illuminated by two parallel rays denoted as 'Ray 1' and 'Ray 2'. Both rays are in phase at the wavefronts A and B. The figure is adapted from [7].

When two parallel lights are incident on a diffraction grating, the path difference between rays becomes $d\sin\alpha + d\sin\beta$ where the angle β , and $\sin\beta$ as well, is negative due to the sign convention. Since the parallel rays are in phase at the wavefront of B, the path difference between them should be equal to the wavelength of the light or multiple of λ . Remainder angles lead to destructive interference. As a result, we obtain the grating equation as 220 where m is the diffraction order.

$$m\lambda = d (\sin\alpha + \sin\beta) \quad (220)$$

The grating equation of 220 is available for the rays that are perpendicular to grooves. In the case where rays are incident on grooves by an angle, the equation 221 becomes valid where ε refers to the angle between the path of incident light and the plane perpendicular to grooves [7].

$$m\lambda = \cos(\varepsilon) d (\sin\alpha + \sin\beta) \quad (221)$$

The grating equation results in more than one diffraction angle β which means that diffraction orders occur. The condition of $\frac{\lambda}{d} \ll 1$ results in many diffraction orders. For instance, for one wavelength, we have positive first diffraction order ($m = 1$), and

negative first diffraction order ($m = -1$). For positive orders, m is larger than 0 and $\beta > -\alpha$. For negative orders, m is smaller than 0 and $\beta < -\alpha$. The special case is the refraction case which makes $\beta = -\alpha$.

2.1.5 Diffractive Optical Elements (DOEs) and SpliCon

Diffractive optical elements (DOEs) are a type of diffraction grating utilized in different applications through a microstructured surface. The basis application of a DOE is to manipulate the incident light on it to alter the phase or amplitude of the light. Via utilization of DOEs, manipulation of light that cannot be achieved by refractive optics can be succeeded. In addition to that, their compact structure gets the chance to replace the designs with bulky, complex and expensive systems.

DOEs can be categorized as amplitude modulation and phase modulation. Amplitude elements alter the intensity of incident light by transmitting a certain percentage while absorbing or reflecting the remaining percentage [8]. Phase elements have a more complex way of working. They transmit the whole intensity of the incident light, but apply a periodic phase delay to the incident light by either periodically altering the refractive index of the material or changing the physical thickness of the material [8]. For a given discrete wavelength, phase elements are advantageous, because they can diffract 100% of the incident light to one diffraction order.

Assume that d is the spacing of grooves, T is the thickness of the grooves, n is the refractive index of the material and A_m is the amplitude of the diffracted light of m^{th} diffraction order in the equation 222.

$$A_m = \frac{\sin\left(\pi d \left(\beta - \frac{m}{d}\right)\right)}{\pi d \left(\beta - \frac{m}{d}\right)}, \beta = \frac{(n-1)T}{\lambda d} \quad (222)$$

Therefore, the diffraction efficiency of the grating at m^{th} diffraction order is found as the equation 223. Diffraction efficiency is defined as the magnitude of a ray that is diffracted to the desired position relative to the magnitude of the other diffracted rays [38].

$$\eta_m = \left[\frac{\sin\left(\pi d \left(\beta - \frac{m}{d}\right)\right)}{\pi d \left(\beta - \frac{m}{d}\right)} \right]^2 \quad (223)$$

The diffraction efficiency of the first order is found as 224. If $\beta = \frac{1}{d}$ in the equation, the diffraction efficiency on the first diffraction order becomes 100%.

$$\eta_1 = \left[\frac{\sin(\pi(\beta d - 1))}{\pi(\beta d - 1)} \right]^2 \quad (224)$$

The diffraction efficiency can be at its maximum when $T = \frac{\lambda_0}{(n-1)}$ for a design wavelength of λ_0 which converts equation 224 to equation 225. As a result, the diffraction efficiency is 100% at the design wavelength λ_0 , and shifts to smaller values as the wavelength deviates from the design wavelength.

$$\eta_1 = \left[\frac{\sin\left(\pi\left(\frac{\lambda_0}{\lambda} - 1\right)\right)}{\pi\left(\frac{\lambda_0}{\lambda} - 1\right)} \right]^2 \quad (225)$$

The average diffraction efficiency over a specific wavelength interval of $\lambda_0 \pm \Delta\lambda$ is given by 226.

$$\bar{\eta}_1 = \frac{1}{\Delta\lambda} \int_{\Delta\lambda} \eta_1(\lambda) d\lambda \approx \left[1 - \left(\frac{\pi\Delta\lambda}{6\lambda_0} \right)^2 \right] \quad (226)$$

This type of DOE is relatively hard to fabricate due to the varying phase profile every 2π phase interval [8]. An easier to fabricate DOE structure is a multi-level phase structure as in Fig. 2.8. Multi-level phase structure has repeating phase values such as 2, 4 or 8 discrete phase values.

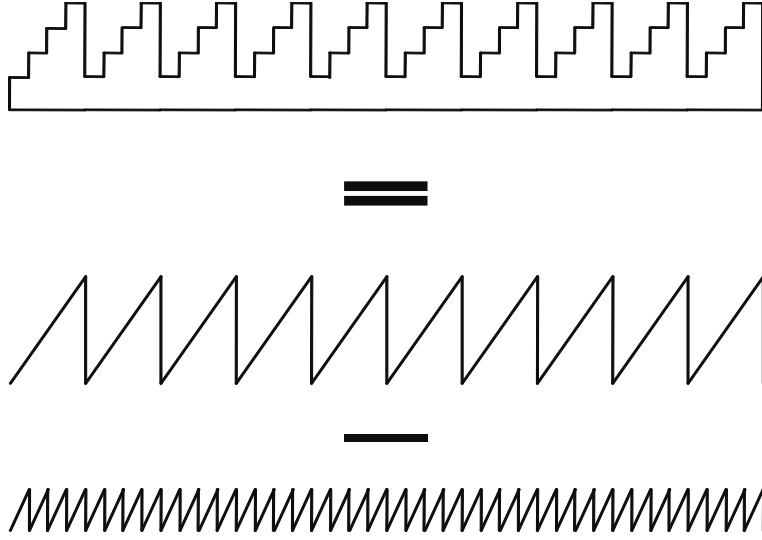


Figure 2.8: A DOE with varying discrete height values can be represented as the difference between two phase structures. The figure is adapted from [8].

The diffraction efficiency of a multi-level phase structure at any wavelength for any diffraction order is given in equation 227 where N is the number of discrete phase levels.

$$\eta_m^N = \left[\frac{\sin \left(\pi \left(\frac{(n-1)T}{\lambda} - m \right) \right)}{\left(\pi \left(\frac{(n-1)T}{\lambda} - m \right) \right)} \right]^2 \left[\frac{\sin \left(\pi \left(\frac{(n-1)T}{\lambda N} \right) \right)}{\left(\pi \left(\frac{(n-1)T}{\lambda N} \right) \right)} \right]^2 \quad (227)$$

The diffraction efficiency is closer to 100% as the number of discrete phase values increases. If we implement corresponding values for a 16-phase level to the diffraction efficiency equation, the diffraction efficiency becomes 99% at the first diffraction order where the remaining part is diffracted into the higher diffraction orders.

The resulting wave after the grating is $f(x,y,0) = U(x,y)p(x,y)$ where $p(x,y)$ is the aperture function which equals 1 inside the aperture, and equals to 0 outside the aperture. According to the thin element approximation, the diffraction inside the diffractive material is neglected, which means that $p(x,y) = 1$, and the propagation direction does not change through the material [39]. The phase delay caused by the optical path length difference due to varying thickness through the diffractive material is defined by the equation 228 where $\phi(\lambda)$ is the phase difference between the incident light passing through the phase element and incident light passing through no phase element, h and $n(\lambda)$ are the thickness and the refractive index of the phase element, respectively [40].

$$\phi(\lambda) = \frac{2\pi}{\lambda} h [n(\lambda) - 1] \quad (228)$$

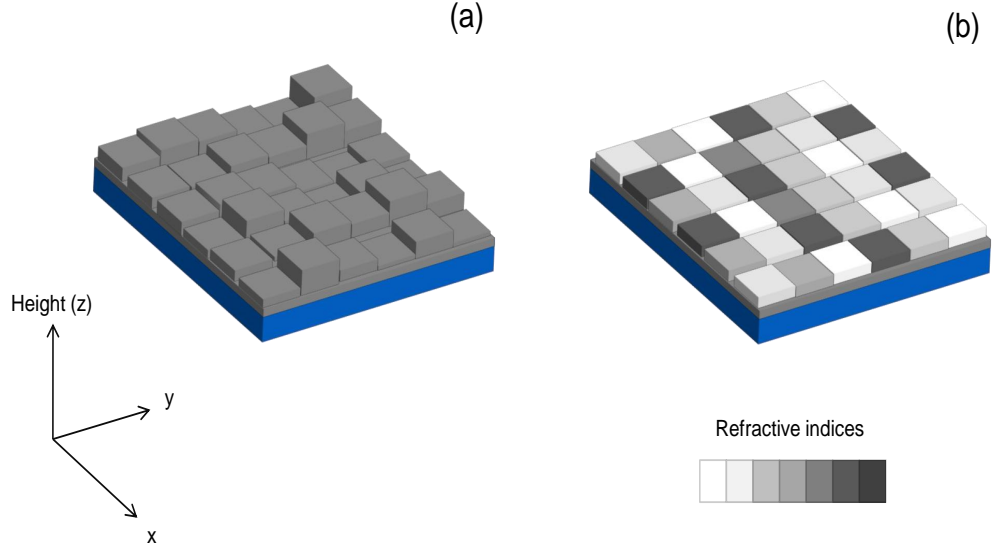


Figure 2.9: (a) A DOE with seven varying height values, and (b) the surface of the SLM with seven varying refractive indices. While both DOE and SLM have the same dimension along the x and y directions, the height value of DOE changes along the z direction.

In the case of DOE, the refractive index of the phase element is constant while the thickness of the phase element changes. In the case of SLM, we have a varying refractive index of the phase element while the thickness of the phase element is constant as in Fig. 2.9. By the equation 228, the gray value encoded on the surface of the SLM can be transformed to a physical DOE. A particular type of DOE that spectrally splits and concentrates the broadband light to sub-bands is called a SpliCon.

CHAPTER 3

INSTRUMENTATION AND METHODS

3.1 The Experimental Setup

The light source used in the experiment is a stabilized fiber-coupled broadband light source SLS201L that is working in the range between 360-2600 nm from Thorlabs. It is a halogen-tungsten bulb light source that has fewer infrared photons as compared to visible range photons [25]. The light source can be used with a fiber linked with an SMA connector or free-space output. The biggest drawback of fiber-coupled output is the power drop which reduces the intensity afterward. After leaving the light source, the light passes through an ACL 25416U-A aspheric condenser lens which is suitable for collimating the light from a light source similar to ours. After passing through the aspheric condenser lens, the light visits PF10-03-M01-10 round protected gold mirror, WP25M-UB mounted wire grid polarizer and another round protected gold mirror, respectively before reaching the SLM surface. Later on, the light is reflected from the SLM surface towards a LA1484 - N-BK7 plano-convex lens that has a focal length of 300 mm. Lastly, the light hits GaAs solar cell which is attached laterally on a copper slab, a Si photodetector with an area of 13 mm² and an InGaAs photodetector with an area of 3.14 mm².

The SLM is connected to the computer where there exists a second virtual screen, and the pattern is encoded on this virtual screen beside the screen we use. The virtual screen has the same size as the SLM surface which is 1920 pixels on the long side and 1080 pixels on the short side. While optimizing an SLM pattern, we optimize a group of pixels which we call superpixels. There are two reasons for using superpixels. In order to optimize all pixels on the SLM surface, which is approximately 2 million pixels, takes 89 days, and the measurement when a single pixel is optimized

is low as compared to the noise level [2]. In addition to these reasons, as the number of superpixels changes, the output also changes.

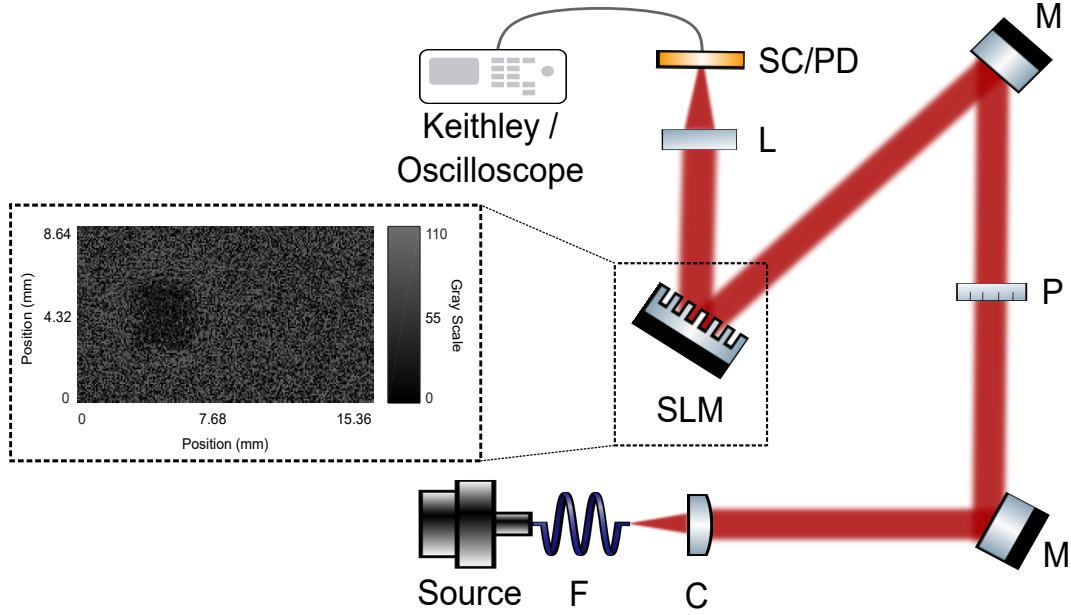


Figure 3.1: The experimental setup to concentrate broadband light on GaAs solar cell and Si/InGaAs photodetectors. A fiber-coupled broadband light goes through a condenser lens with a focal length of 160 mm and a polarizer, and two mirrors. After, the light is reflected to the GaAs and silicon photodetector by a lens with a focal length of 300 mm through the SLM surface. The measurements are obtained through Keithley sourcemeter for GaAs solar cell, and collected by an oscilloscope for photodetectors.

3.1.1 Noise Measurement of the Light Source

The noise measurement for the light source is obtained via a PM100D attached to an S121C standard photodiode power sensor for three hours. Additionally, the measurements are taken one hour after the light source is turned on. S121C standard photodiode power sensor is placed 17 cm away from the condenser lens, and the average power at 671 nm is 2.6 mW. The noise of the light source is 0.3%, which is a suitable value as compared to the typical optical power drift per hour, 0.01% [41]. Noise value is calculated according to the equation 31.

$$\text{Noise (\%)} = 100 \times \frac{\text{Standard Deviation of Measured Power Data}}{\text{Mean Value of Measured Power Data}} \quad (31)$$

We use the light source with a fiber couple. Even though fiber coupling provides more collimated light, it also decreases the power. The power sensor is positioned at 3 cm away, and the power measured when there is no fiber coupling is 44.7 mW. However, the power is 2.85 mW with fiber coupling at the same distance after the fiber. Additionally, the power changes along the setup due to the losses caused by optical elements such as polarizer and SLM. The power measured before the polarizer is 0.283 mW, while the power of the light source drops to 75 μ W after, and it also decreases to 3.64 μ W after the SLM.

3.1.2 Spatial Light Modulator (SLM)

A Spatial light modulator (SLM) is a liquid crystal based electrical device where the wavefront of the light is modulated by controlling the voltage of the liquid crystal material inside. Phase, polarization state, amplitude and propagation direction, or a combination of four of them can be modulated.

The internal structure of SLM consists of a liquid crystal layer on top of a silicon substrate, and an electrode layer on top of a glass substrate. The pixel electrodes inside this layer are made of aluminum where the potential difference of electrodes is controlled separately. Between the silicon substrate and a glass substrate, there exists a liquid crystal material attached to pixel electrodes aligned parallel to both of the layers. This pixel-wise structure and liquid crystal materials also lead to an efficiency loss because of diffraction and scattering of the light, respectively [9].

The potential difference across the liquid crystal material is altered pixel by pixel independently so that the liquid crystal material inclines to result in a refractive index difference and an optical path length change in the liquid crystal material. Therefore the phase of incident light gets modulated. The liquid crystal material is aligned parallel to the glass layers when there is no applied voltage.

It is important to have linearly polarized incident light while the polarization direction of incident light should be parallel to the direction of the liquid crystal material

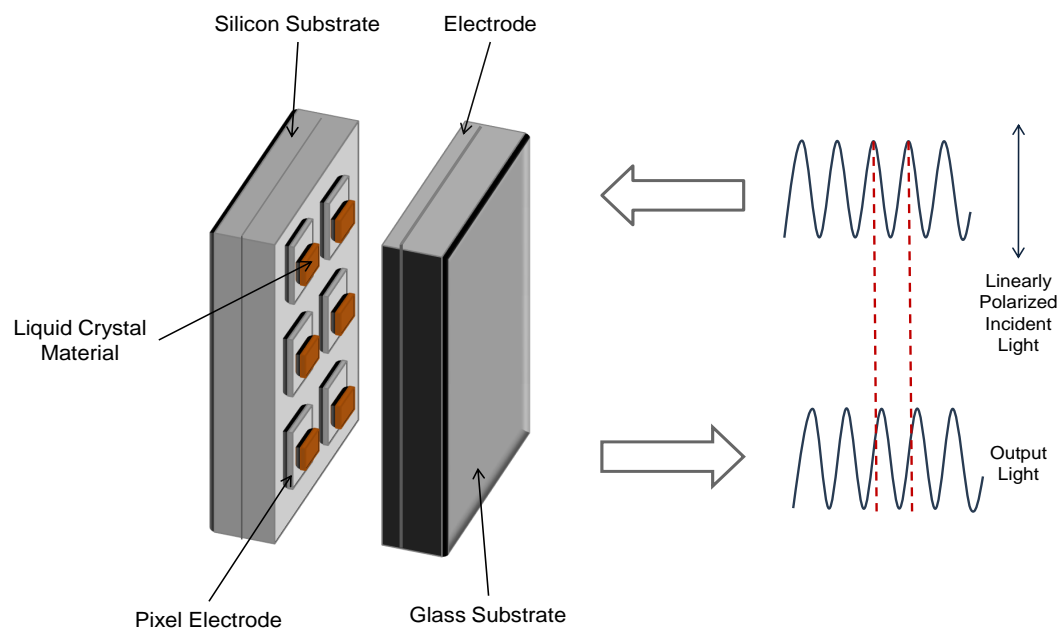


Figure 3.2: A schematic representation of layers of the SLM where each LC material is attached to an electrode. The figure is adapted from [9].

without a voltage applied. Otherwise, there is no modulation of the phase of incident light after it passes through the SLM. There are various applications of SLM covering optical tweezers [42], beam steering [43, 44], programmable adaptive optics [45], polarization modulation [46] and microscopy [47] which need a fast modulation of wavefront of the incident light.

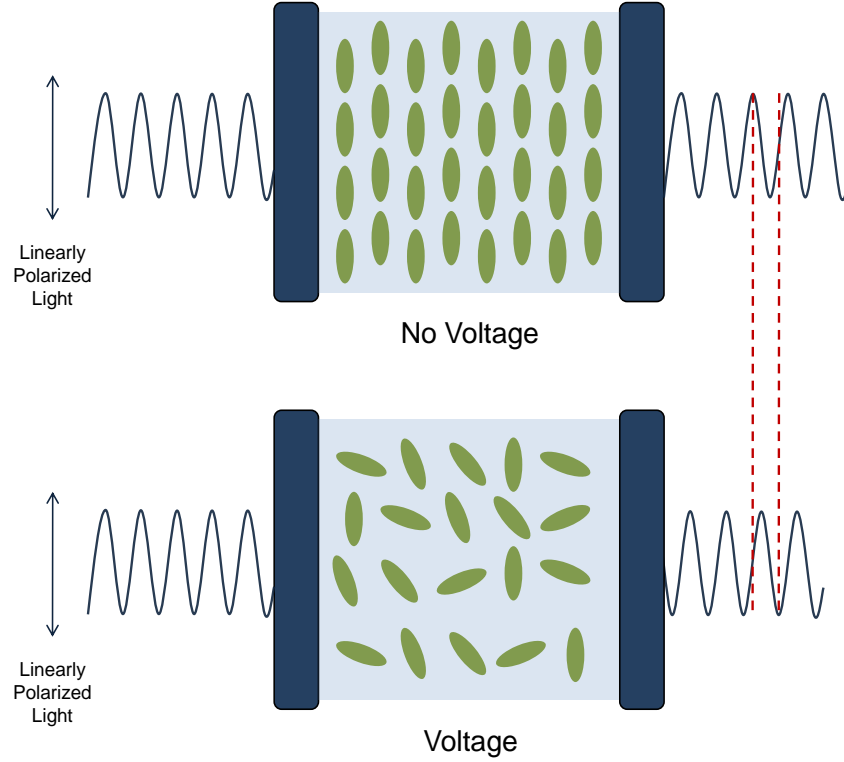


Figure 3.3: LC materials aligned parallel to the both substrates without voltage, and a tilted direction of alignment of LC material with an applied voltage resulting in a phase modulation, respectively.

3.1.3 Characteristics of the GaAs Solar Cell

Fig. 3.4 shows the structure of the GaAs solar cell. The cell samples are fabricated via Veeco GEN20 molecular beam epitaxy (MBE) system. The layer of n+ doped GaAs has 200 nm thickness and a doping concentration of $3 \times 10^{18} \text{ cm}^{-3}$, n+ doped

$\text{Al}_{0.3}\text{Ga}_{0.7}\text{As}$ has a doping concentration of $3 \times 10^{18} \text{ cm}^{-3}$ and 30 nm thickness, n-doped GaAs has 3200 nm thickness and a doping concentration of $1 \times 10^{17} \text{ cm}^{-3}$, p+ GaAs has a doping concentration of $2 \times 10^{18} \text{ cm}^{-3}$ and 150 nm thickness, p+ $\text{Al}_{0.8}\text{Ga}_{0.2}\text{As}$ has 45 nm thickness and a doping concentration of $3 \times 10^{18} \text{ cm}^{-3}$, and p++ GaAs has a doping concentration of $5 \times 10^{18} \text{ cm}^{-3}$ and 148 nm thickness. Under the AM1.5 illumination condition, GaAs solar cell has 980 mV of open circuit voltage, $\sim 31 \text{ A/cm}^2$ of short circuit current density, 20.8 W of maximum power, 740 mV of MPP voltage (V_{mp}) and $\sim 28 \text{ A/cm}^2$ of MPP current density (J_{mp}) under the same illumination condition. The fill factor and the efficiency of the solar cell are measured as $\sim 70\%$ and $\sim 9\%$, respectively. Fig. 3.6 shows the transmittance spectrum and the absorbance spectrum of GaAs solar cell.

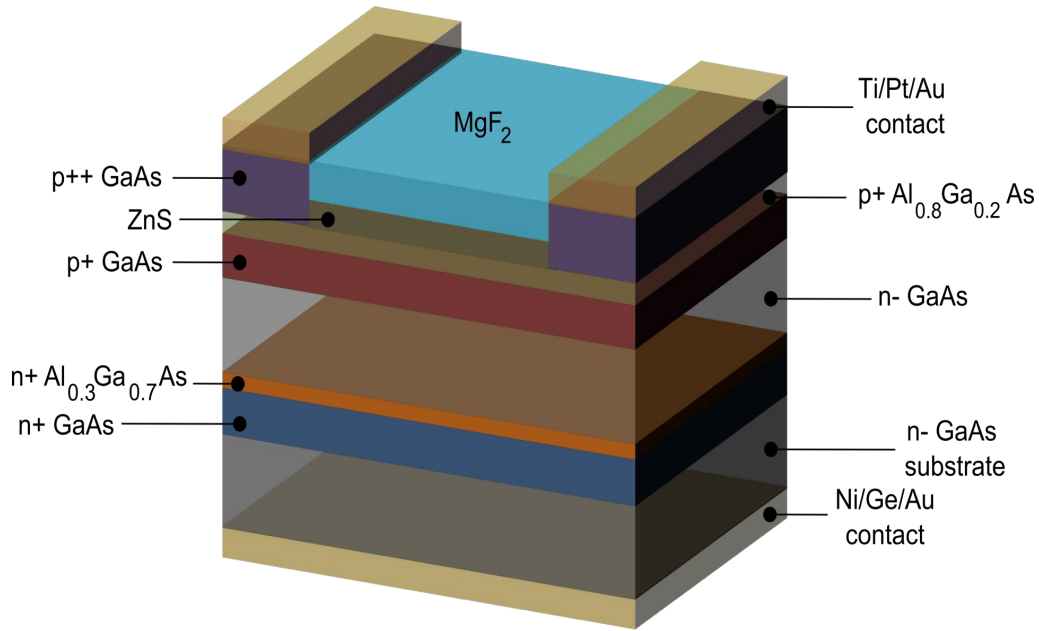


Figure 3.4: Fabricated GaAs solar cell via molecular beam epitaxy where the doping and material types are shown.

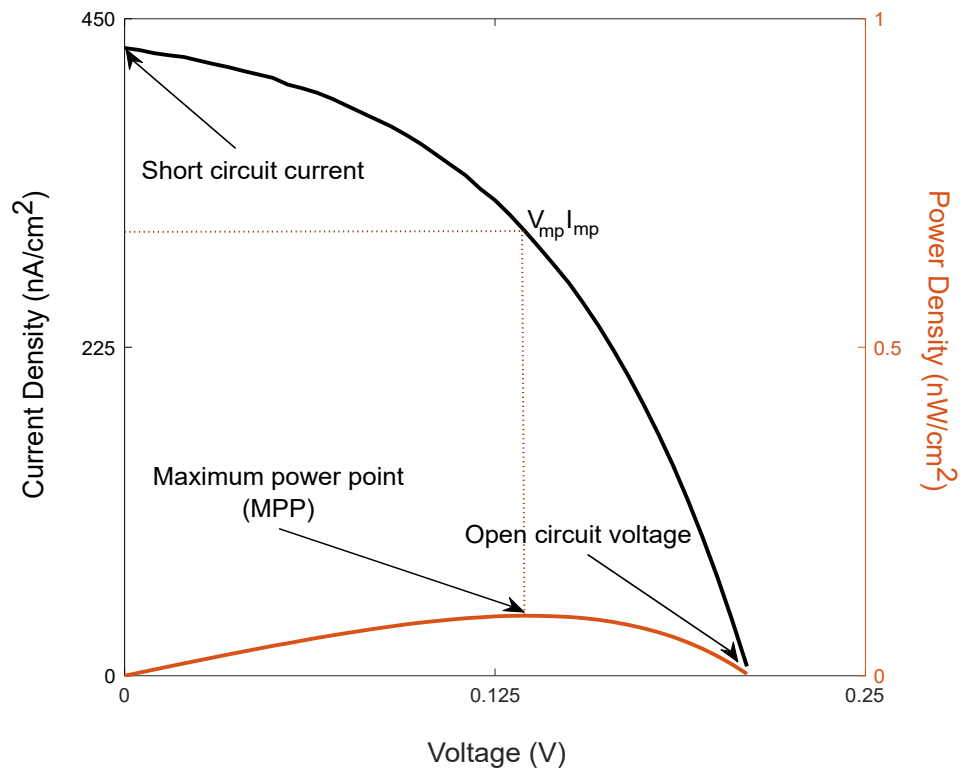


Figure 3.5: Typical IV curve of a solar cell. Solar cell characteristics are denoted on the graph which are short circuit current, open circuit voltage and maximum power point (MPP).

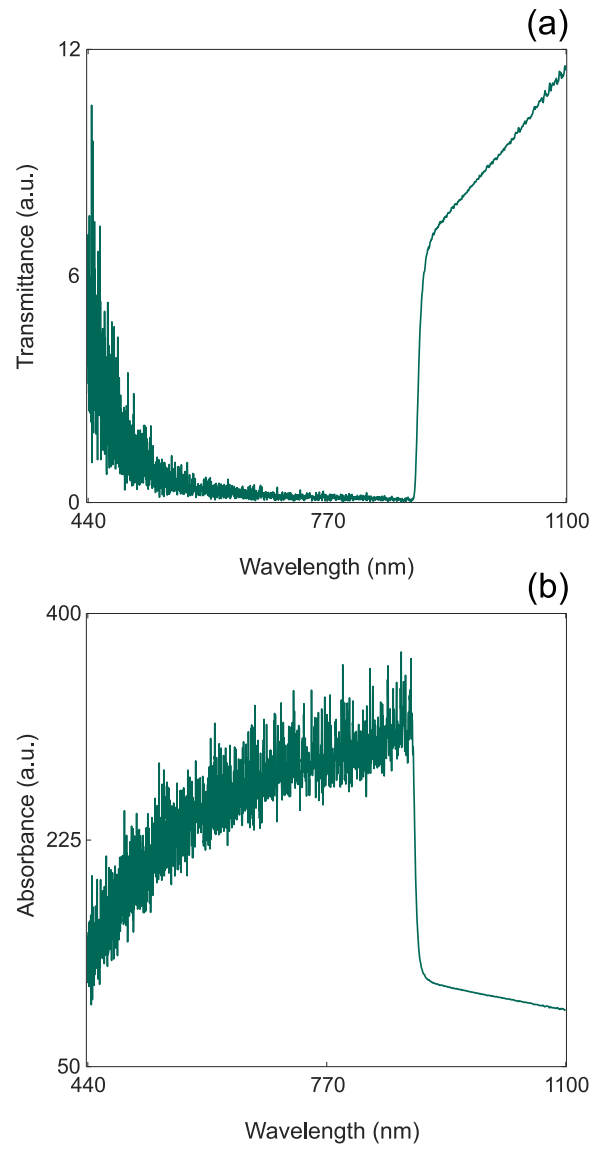


Figure 3.6: (a) Transmittance spectrum and (b) absorbance spectrum of GaAs solar cell with respect to wavelength in between 300 nm and 1000 nm.

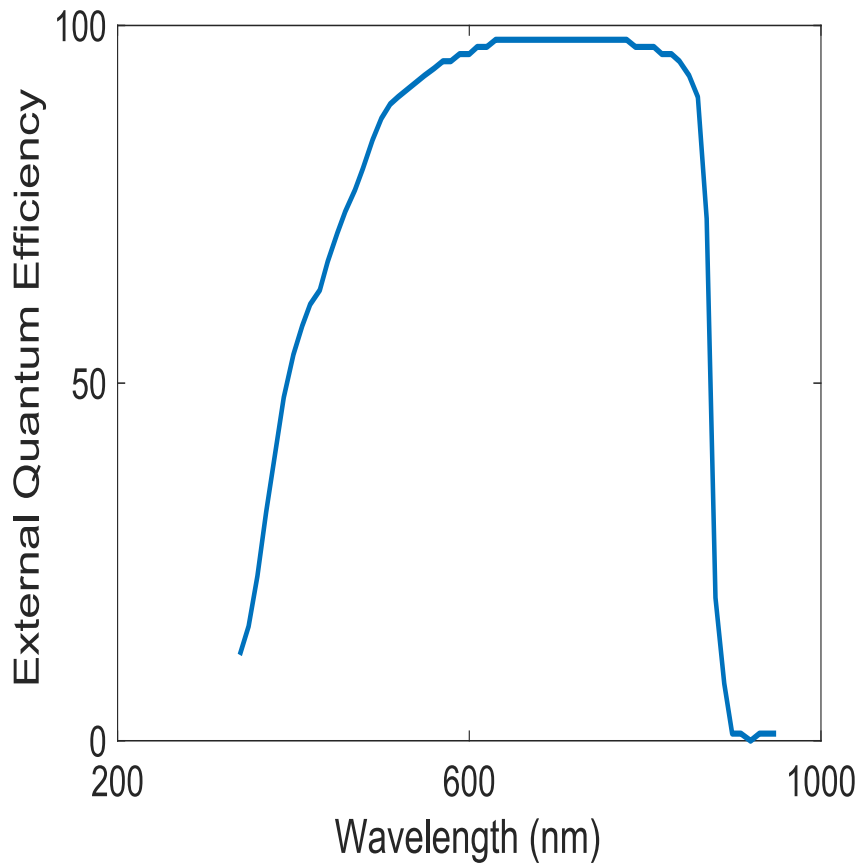


Figure 3.7: External quantum efficiency of GaAs solar cell with respect to wavelength in between 440 nm and 1100 nm.

3.2 Sourcemeter Connection

The current measurement for GaAs solar cell is achieved by 2-wire measurement and 4-wire measurement. We use Keithley 2440 sourcemeter for 4-wire measurement to apply a bias and measure the current through solar cells simultaneously.

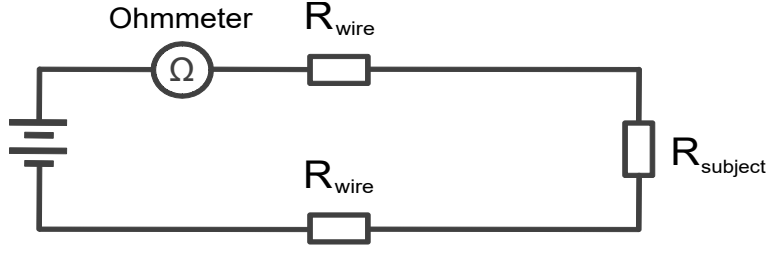


Figure 3.8: The circuit which represents 2-wire measurement.

With a typical ohmmeter, 2-wire measurement seen in Fig. 3.8 is implemented where the resistance of a subject is measured from a distance. Ohmmeter forces a current that is called the test current through the circuit, measures the voltage drop and calculates the resistance. However, while forcing the test current to the circuit, it forces current along both wires and the subject, resulting in a voltage drop on wires too. While the resistance of wires is small, it contributes to the measurement errors if the subject is positioned at a distance and wires are long, or the measured subject has a very low resistance [48]. In the equation 32, V_m and I refers to the voltage read from meter and test current, respectively. The resistance of wires is added to the measured resistance for 2 wire-measurement.

$$\text{Measured resistance} = \frac{V_m}{I} = R_{\text{subject}} + (2 \times R_{\text{wire}}) \quad (32)$$

In order to eliminate the error caused by the resistance of wires, a 4-wire measurement is performed as seen in Fig. 3.9. There are four connections where two come from the source which are called force leads, and two come from the voltmeter which are called sense leads. In this configuration, the test current is forced through force leads, and causes a voltage drop on those wires. Moreover, the subject is directly attached to the voltmeter where the wires have a negligible voltage drop. As a result, the voltage drop on the subject and the voltage that is read on the voltmeter are almost identical which means that the resistance of wires is eliminated. In the meantime, there are some drawbacks of 4-wire resistance. It slows down the measurement, and adds more wires and a number of test points [49]. In the equation 33, V_m , V_R and I refers to the voltage read from meter, the voltage drop on the subject and test current, respectively. Since V_m and V_R are almost equal, only the resistance of the subject is measured on voltmeter.

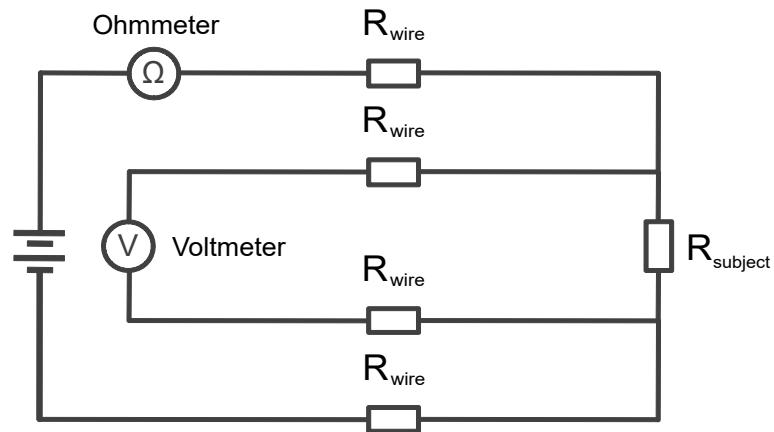


Figure 3.9: The circuit which represents 4-wire measurement where the resistance of wires that are attached to the voltmeter are in the order of picoamperes, thus they are negligible.

$$\text{Measured resistance} = \frac{V_m}{I} = \frac{V_R}{I} = R_{\text{subject}} \quad (33)$$

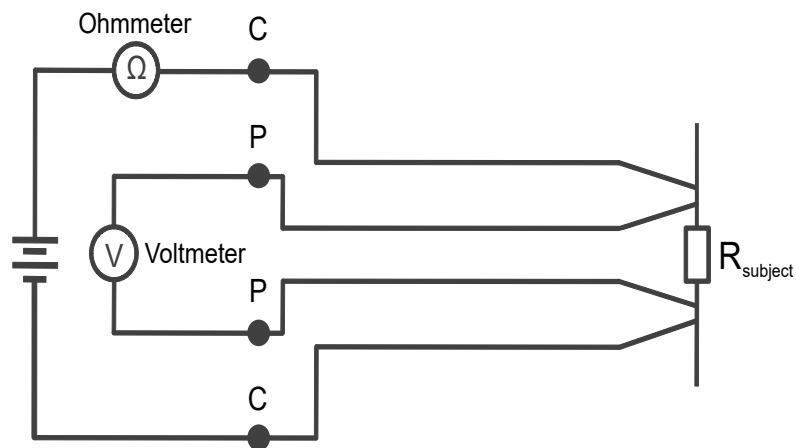


Figure 3.10: Representation of Kelvin probes which are attached to a sourcemeter connection. "C" represents the wire where the test current is forced, while "P" represents the potential where the measurement is carried out. The cables of Kelvin probes are insulated from each other, and may only contact to each other on the terminals of the subject.

Kelvin probes are connected to the cables that are out of the Keithley 2440 sourceme-
ter. The cables attached to the terminal of probes are insulated from each other, and
only terminal points of probes contact where they clasp the anode and cathode of the
subject. Consequently, in Fig. 3.10, the current through "C" which is called the test
current, does not go through "P" where the measurement is carried out. As a result,
the current passes through "P" is negligible, and does not cause a significant voltage
drop on "P" wires.

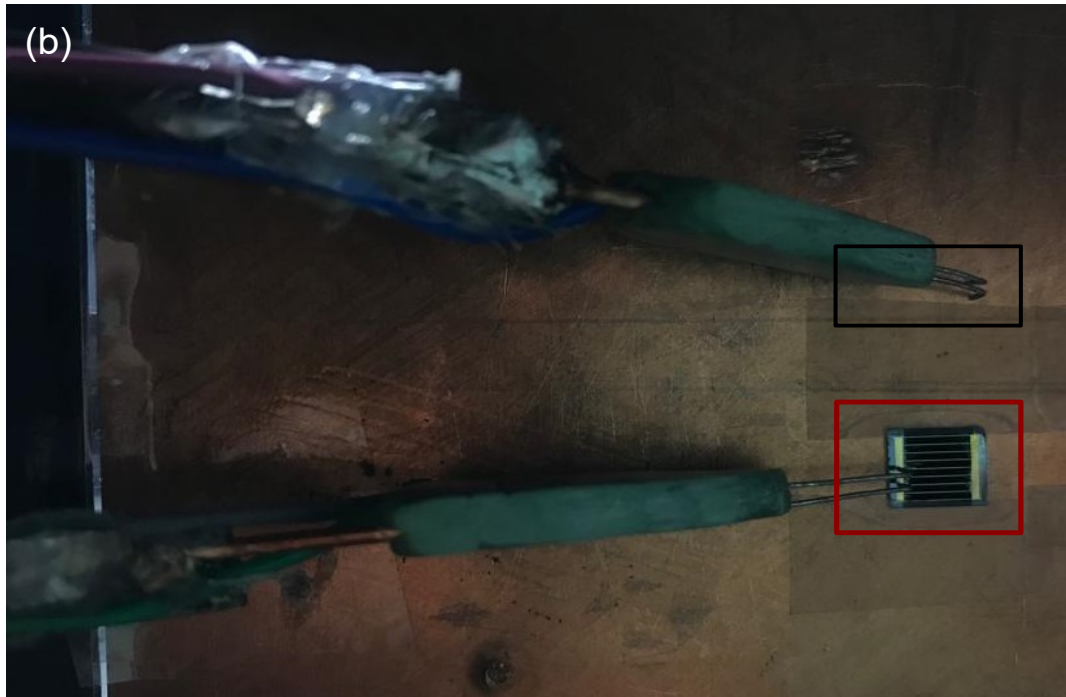
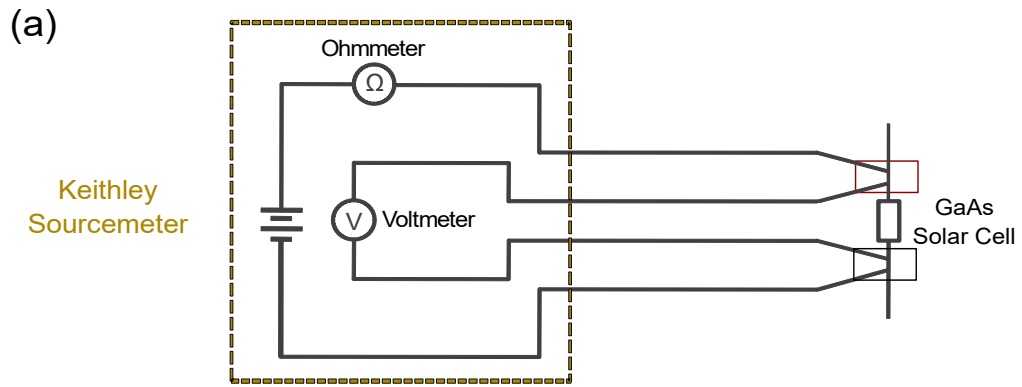


Figure 3.11: (a) The schematic representation of Keithley 2440 model. (b) The platform for solar cell measurement including GaAs solar cell that is placed on a copper plate, and Kelvin probes connected to Keithley 2440 on the left side and contacted to the terminals of GaAs on the right side. Copper plate where the GaAs solar cell is attached behaves as negative of the solar cell. The black box shown in (a) is attached to the copper plate, and the red box shown in (a) is attached to anode of the GaAs solar cell.

3.3 The Optimization Algorithm

The algorithm performs iterative scanning of each superpixel on the surface of the SLM. 8-bit black value at each superpixel on a visual screen is written on the surface of the SLM by the algorithm which means there is no modulation yet. Subsequently, the algorithm starts to encode 10 separate phase differences by increasing 11 steps to each superpixel by starting from the left top edge of the SLM surface via the visual screen. Each phase difference corresponds to a distinct gray value.

The GaAs solar cell is positioned in the middle of the incoming beam, and the current value that is read from the cell for a specified bias is obtained via Keithley sourceme-ter. Similarly, Si/InGaAs photodetectors are positioned in the middle of the incoming beam, and the RMS values are obtained from an oscilloscope.

According to the measured and recorded current values, the algorithm scans the gray values, and writes the one gray value giving the highest current measured. This scanning process of one superpixel is called sub iteration which takes 250 ms. After writing one gray value for one superpixel, the algorithm continues to scan the next right-hand superpixel. After whole superpixels on the SLM surface are assigned a gray value, a phase pattern is obtained on the SLM surface, which is called the main iteration. As the number of superpixels increases, the optimization time also increases. For 2304 superpixels, the optimization time takes 2 hours while for 20736 superpixels, it takes 18 hours.

CHAPTER 4

RESULTS AND DISCUSSION

4.1 Spectral Splitting and Concentration of the Broadband Light on the CCD Camera

The broadband light (360 - 2600 nm) is concentrated and split into two sub spectrums on the CCD camera via SLM. In the setup, there is a CCD camera on the position of GaAs solar cell or Si/InGaAs photodetector, and the measured value is the intensity value of red, green and blue channels. The center position for red channel is decided as $(x,y) = (1.3 \text{ mm}, 1.9 \text{ mm})$, and for blue and green channels as $(x,y) = (3.5 \text{ mm}, 1.9 \text{ mm})$ as seen in Fig. 4.1. The resulting pattern is a SpliCon which split the broadband light and concentrates the sub bands into the solicited positions.

The enhancement factor of the image is defined as the equation 41 for each channel where A_m is the area of the target region ($m=1, 2, 3, \dots$), and $\int_T I_f(A_m, \lambda) dA_m$ and $\int_T I_i(A_m, \lambda) dA_m$ are the intensities of CCD image on the target area after the modulation and before the modulation, respectively [2]. Enhancement factor for red channel is calculated as 3.7 at the target position, and calculated as 4.6 and 3.6 for green channel and blue channel at the target position for 20736 superpixels, respectively.

$$\eta(\lambda) = \frac{\int_T I_f(A_m, \lambda) dA_m}{\int_T I_i(A_m, \lambda) dA_m} \quad (41)$$

The splitting ratio which is the ratio of spectral intensity on the target position over the spectral intensity on both target positions is found via the equation 42 [2]. The splitting ratio is calculated as 45% for the red channel, and calculated as 58% and 64% for the green channel and the blue channel at the target position for 20736 superpixels, respectively.

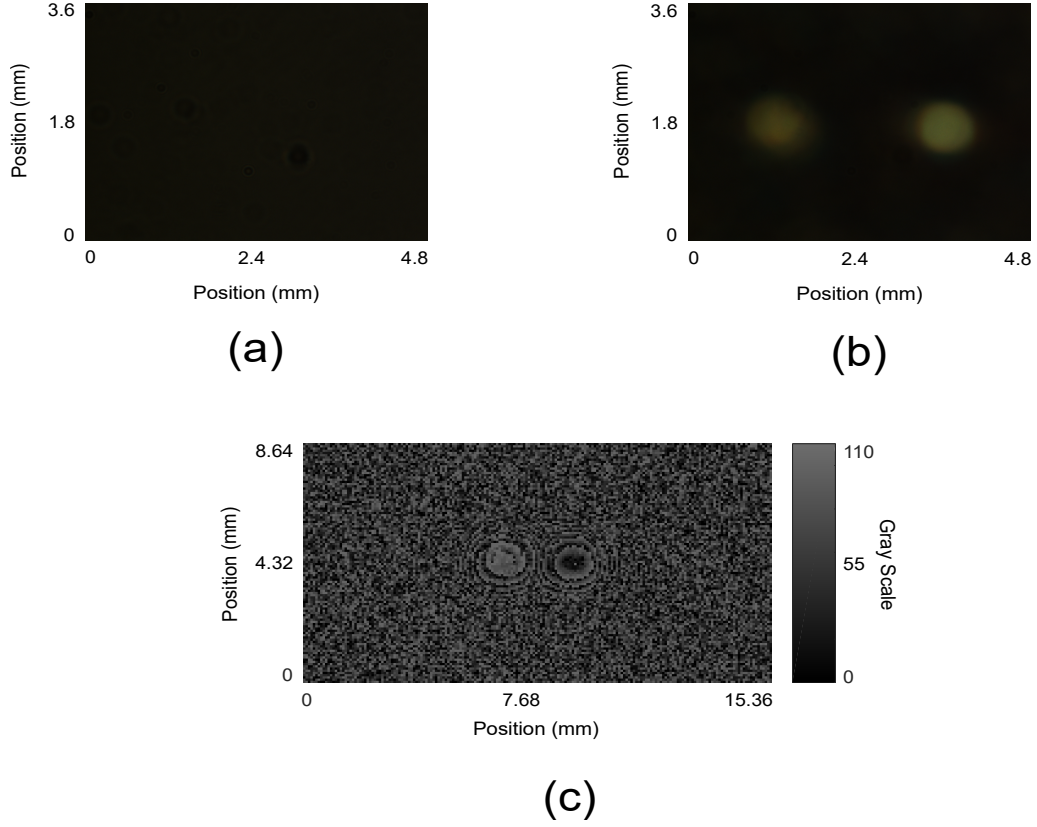


Figure 4.1: The CCD image (a) before the optimization of the SLM surface, (b) after the optimization of the SLM surface to concentrate light on the desired positions and (c) resulting phase pattern on the SLM surface to split and concentrate the broadband light on desired positions. Red channel is concentrated from $(x,y) = (1.11 \text{ mm}, 1.7 \text{ mm})$ to $(x,y) = (1.48 \text{ mm}, 2.1 \text{ mm})$, and green and blue channels are concentrated from $(x,y) = (3.34 \text{ mm}, 1.7 \text{ mm})$ to $(x,y) = (3.71 \text{ mm}, 2.1 \text{ mm})$.

$$S(\lambda) = \frac{\int_T I_f(A_m, \lambda) dA_m}{\sum_{m=1} \int_T I_i(A_m, \lambda) dA_m} \quad (42)$$

As the number of superpixels changes, the enhancement factor and splitting ratio value alternate as well. Fig. 4.2 shows the different enhancement factors and splitting ratios for each channel according to the number of superpixels. For the red, green and blue channels, the enhancement factor rises with an increasing number of superpixels. The splitting ratio of the green and blue channels increases with an increasing number of superpixels. On the other hand, the splitting ratio of the red channel drops as the number of superpixels increases.

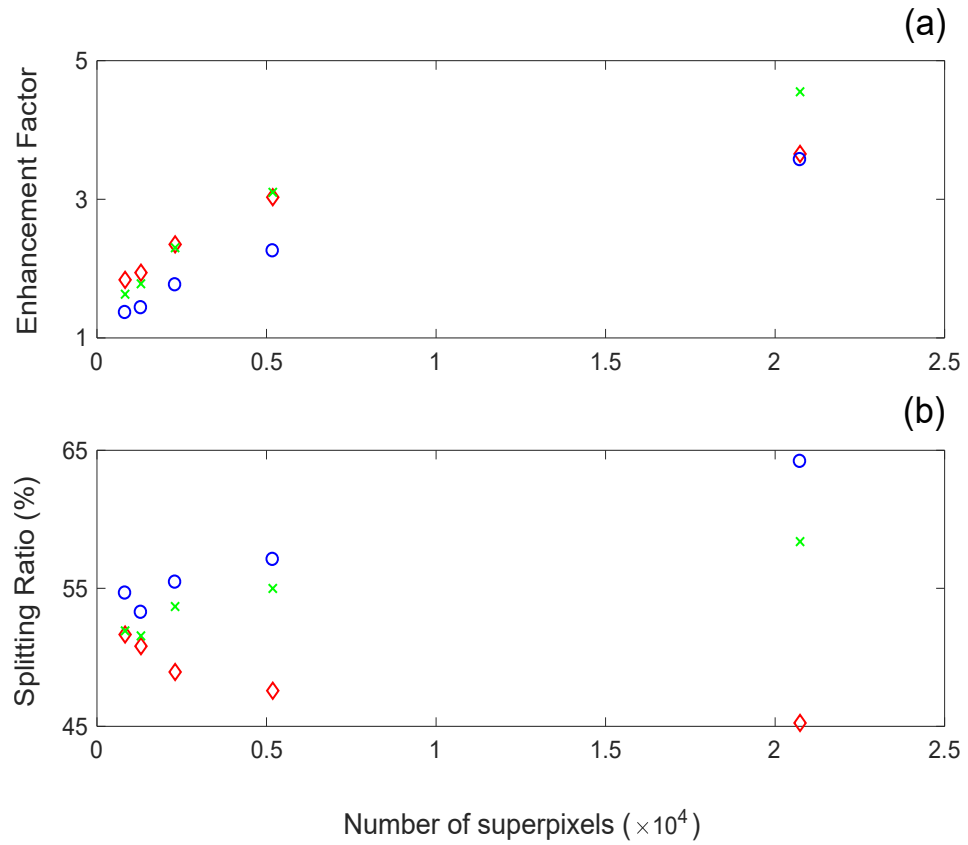


Figure 4.2: Varying (a) enhancement factors and (b) spectral splitting ratios according to the different number of superpixels for the red channel, the green channel and the blue channel.

4.2 Enhancing Performance of the GaAs Solar Cell via Wavefront Shaping

The concentration of broadband light on GaAs solar cell is achieved on the setup 3.1 where GaAs solar cell is attached to a Keithley sourcemeter to apply a bias and measure the corresponding current simultaneously.

4.2.1 Reference and Noise Measurements of GaAs

According to the measurements that are taken under 1 sun (100 mW/cm^2), GaAs has an open circuit voltage of 930 mV. Without illumination, the open circuit voltage of the dark current of GaAs is 100 mV. Fig. 4.3 shows the dark and photocurrent for 1 sun illumination. Fig. 4.4 shows the same measurement, but the data is converted to the first quadrant for convenience.

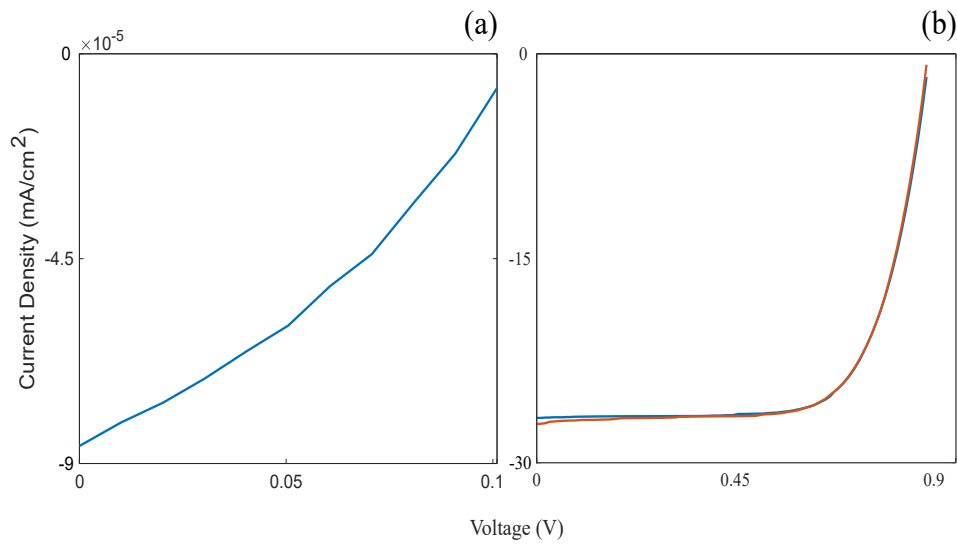


Figure 4.3: The reference (a) dark current density (b) two photocurrent current density measurements for GaAs which are taken under 1 sun illumination.

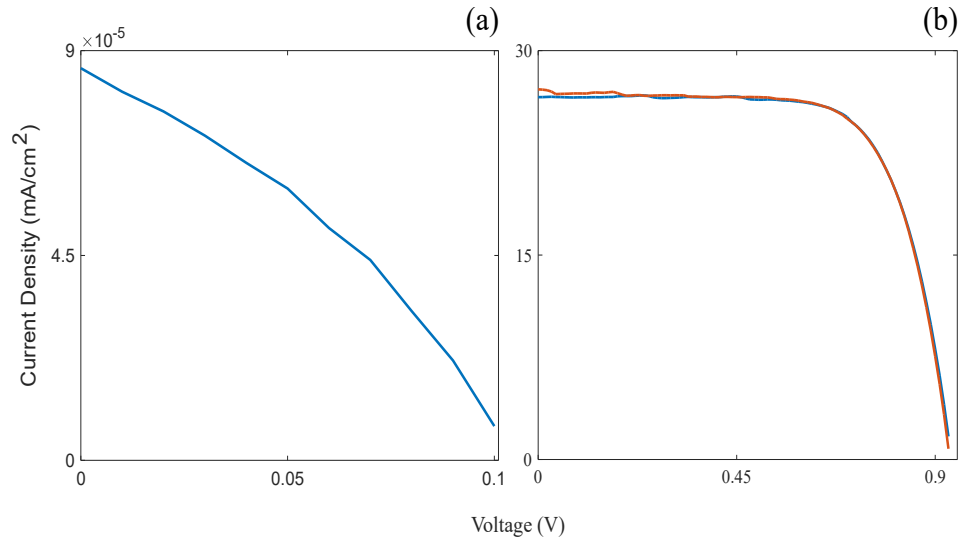


Figure 4.4: The reference (a) dark current density (b) two photocurrent current density measurements for GaAs which are taken under 1 sun illumination, converted to the first quadrant for convenience.

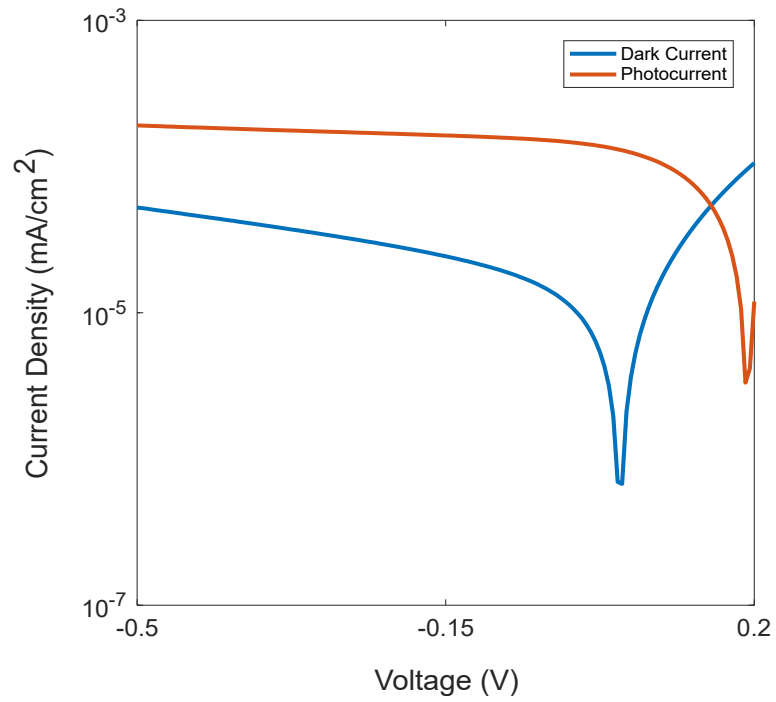


Figure 4.5: The semi-log IV curve of GaAs where the current measured at reverse bias is steady. The optimization bias is chosen as -0.2 V where the noise is 0.5%.

Fig. 4.6 shows the noise measurement data for GaAs is taken for three hours at each

voltage value from -0.5 V to the open circuit voltage value which is 0.19 V with steps of 5 mV. The noise is below 1% at reverse bias, thus the optimization voltage is chosen as -0.2 V where the noise is 0.5%. Additionally, the current measured at reversed bias region is steady as seen in Fig. 4.5, which means that if the sourcemeter applies a different voltage than our optimization voltage, the measured current is not affected drastically by this change. The measurement is taken with the setup in Fig. 3.1.

$$\text{Noise (\%)} = 100 \times \frac{\text{Standard deviation of the current measured}}{\text{Mean value of the current measured}} \quad (43)$$

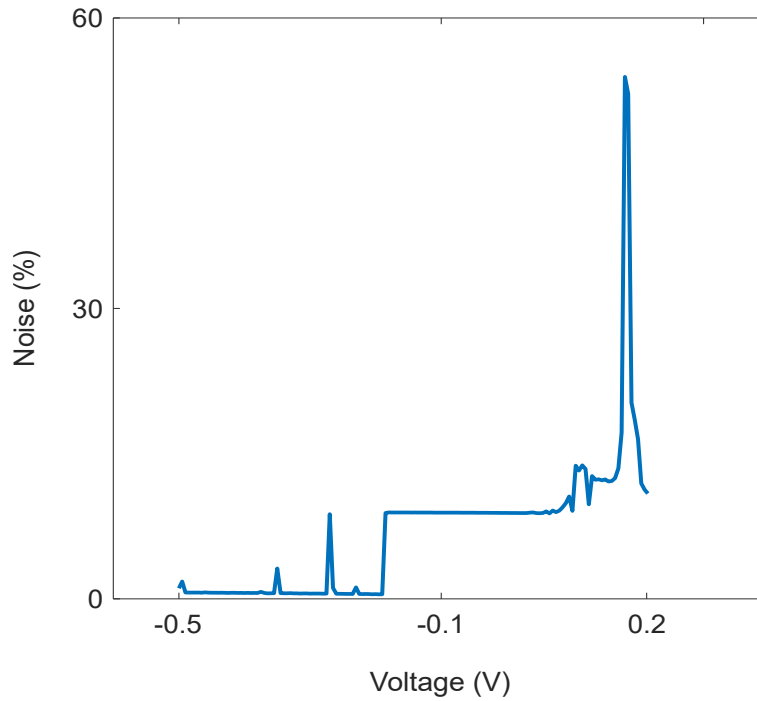


Figure 4.6: GaAs noise measurement is calculated according to the equation 43. It is obvious that the noise is below 1% at the most of reverse bias region.

4.2.2 Achieving Excess Current via Concentration on GaAs

Fig. 4.7 shows the phase patterns which are obtained on the SLM surface for GaAs solar cell. The solar cell is placed in the middle of the beam and the broadband light is concentrated on the solar cell. The structure of the solar cell is clearly seen on the

Number of Superpixels	Excess Current with Dark (%)	Excess Current without Dark (%)
20736	5.86	5.46
5184	9.67	9
2304	10.78	10
1296	9.30	8.67
829	8.35	7.78

Table 4.1: The calculated excess short circuit current of GaAs solar cell for five different number of superpixels.

phase pattern.

$$\text{Excess Current (\%)} = 100 \times \frac{I_{\text{optimization}} - I_{\text{photocurrent}}}{I_{\text{photocurrent}} - I_{\text{dark}}} \quad (44)$$

$$\text{Excess Current (\%)} = 100 \times \frac{I_{\text{optimization}} - I_{\text{photocurrent}}}{I_{\text{photocurrent}}} \quad (45)$$

Excess current at short-circuit current (at 0 V) for GaAs with dark current is found via the equation 44 as 5.86%, 9.67%, 10.78%, 9.30% and 8.35% for 20736 superpixels, 5184 superpixels, 2304 superpixels, 1296 superpixels and 829 superpixels, respectively. In the equation, $I_{\text{optimization}}$ is the current measured after the SLM pattern is reflected on the solar cell, $I_{\text{photocurrent}}$ is the current measured when there is a black pattern on the SLM and I_{dark} is the current when there is no illumination on the solar cell. Nevertheless, the excess current value decreases to negative values after 155 mV due to the dark current being larger than the photocurrent. Therefore, via equation 45, for the calculated excess current, the negative values can be eliminated despite that the excess current value drops a few. Without dark current, the excess current values are 5.46%, 9%, 10%, 8.67% and 7.78% for 20736 superpixels, 5184 superpixels, 2304 superpixels, 1296 superpixels and 829 superpixels, respectively. Fig. 4.8 shows the plot for calculated excess current with and without dark current, respectively. We also achieve an increase of 5 mV at open circuit voltage for 5184 superpixels, 2304 superpixels, 1296 superpixels and 829 superpixels as seen in the Fig. 4.10.

$$\text{Excess Power (\%)} = 100 \times \frac{P_{\text{optimization}} - P_{\text{photocurrent}}}{P_{\text{photocurrent}}} \quad (46)$$

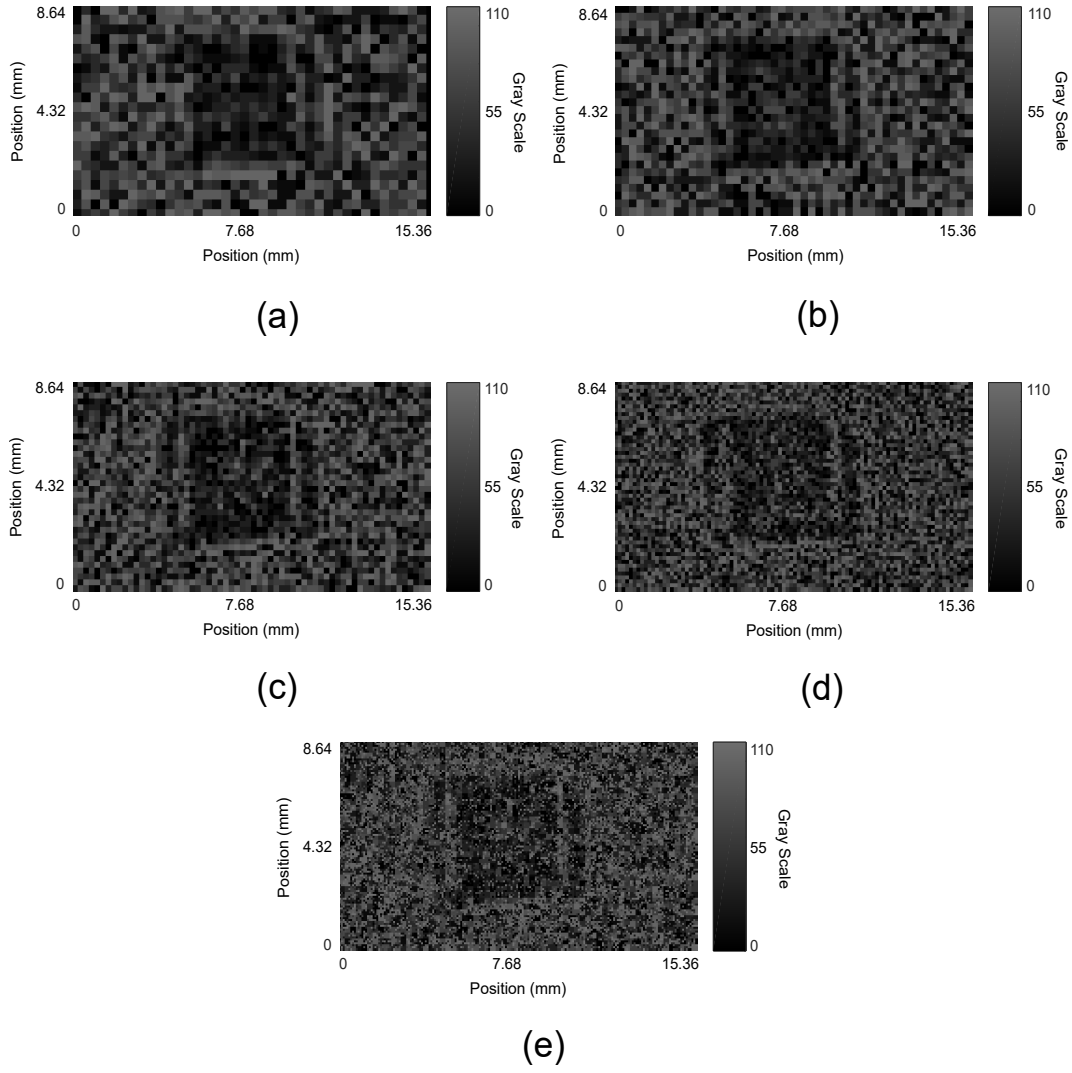


Figure 4.7: SLM phase pattern for GaAs optimized with (a) 829 superpixels (b) 1296 superpixels (c) 2304 superpixels (d) 5184 superpixels (e) 20736 superpixels. The shape of GaAs solar cell is clearly observed on the SLM phase pattern.

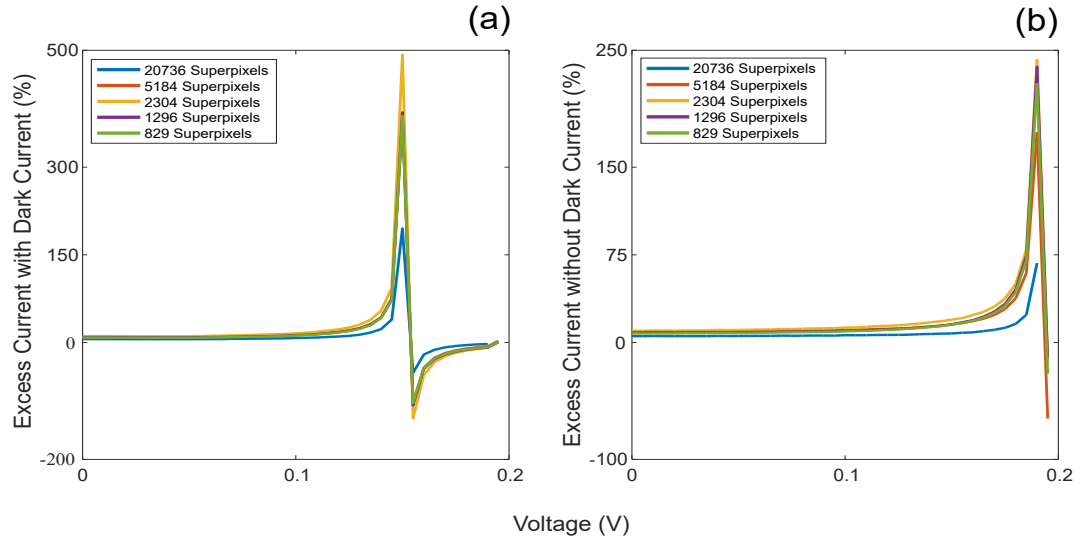


Figure 4.8: Excess current (%) values are plotted with (a) the dark current (calculated via equation 44) and (b) without the dark current (calculated via equation 45).

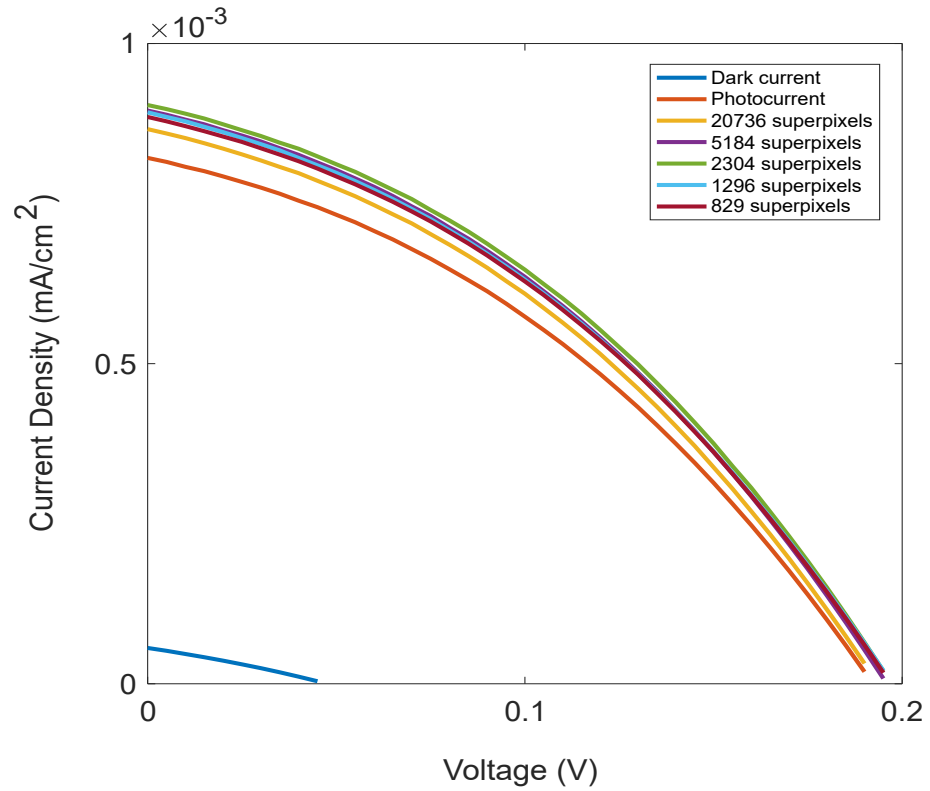


Figure 4.9: The current density vs voltage curve of GaAs solar cell which are taken for the dark current, the photocurrent and current measured for five different number of superpixels. Rise of the short circuit current and the open circuit voltage is clearly seen on the graph.

Number of Superpixels	Excess Current with Dark (%)	Excess Current without Dark (%)
20736	9.43	6.47
5184	16.8	11.52
2304	20.32	14
1296	15.85	10.86
829	15.19	10.41

Table 4.2: The calculated excess current of GaAs solar cell at the maximum power point for five different number of superpixels.

In addition to the calculations above, the current density and the power density increase are calculated at the maximum power point (MPP). The maximum power point is 110 mV for photocurrent, while it rises to 115 mV for a various numbers of superpixels. The excess power is calculated according to the equation 46, and found as 6.44%, 11.5%, 14%, 10.8%, 10.4% for 20736 superpixels, 5184 superpixels, 2304 superpixels, 1296 superpixels and 829 superpixels, respectively. In the equation, $P_{\text{optimization}}$ denotes the power measured when SLM phase plate is reflected on the solar cell, and $P_{\text{photocurrent}}$ denotes when a black pattern is on the SLM surface. The excess current at MPP with dark is calculated as 9.43%, 16.8%, 20.32%, 15.85% and 15.19%, and without dark as 6.47%, 11.52%, 14%, 10.86% and 10.41% for 20736 superpixels, 5184 superpixels, 2304 superpixels, 1296 superpixels and 829 superpixels, respectively.

Number of Superpixels	Excess Power (%)
20736	6.44
5184	11.5
2304	14
1296	10.8
829	10.4

Table 4.3: The calculated excess power of GaAs solar cell at the maximum power point for five different number of superpixels.

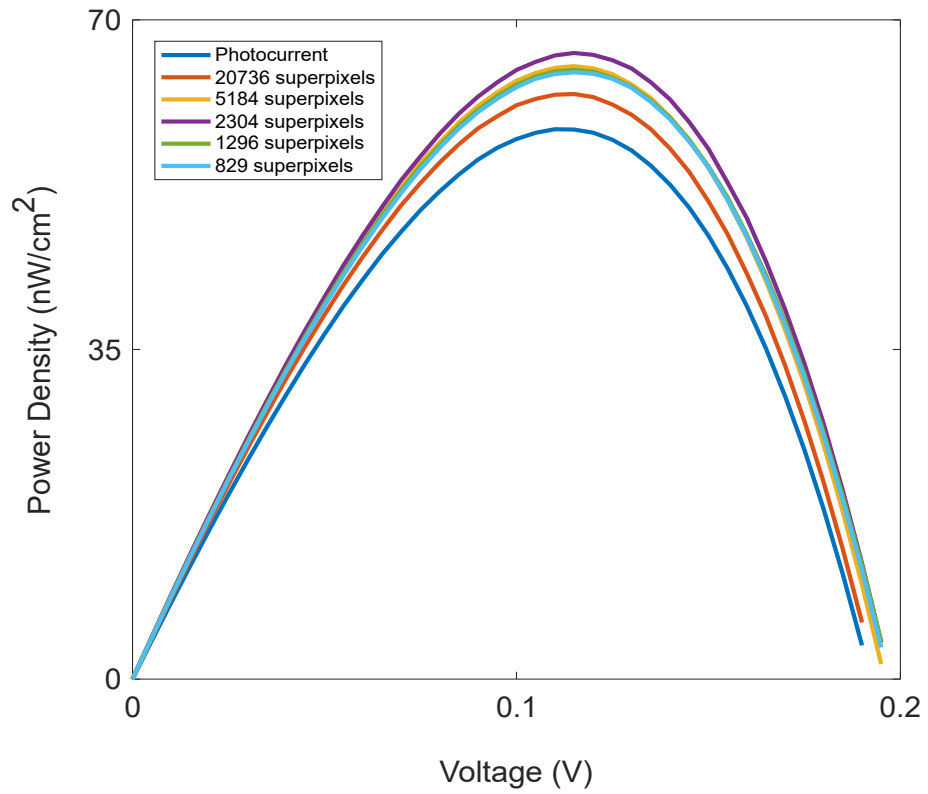


Figure 4.10: The power density vs voltage curve of GaAs solar cell which are taken for the photocurrent and current measured with different number of superpixels. The maximum power point (MPP) shifts to 115 mV from 110 mV for each number of superpixels, and the power density values also increase.

We also investigate the excess current change according to the position of the GaAs solar cell. In the setup, the position of GaAs is changed after the plano-convex lens with a focal length of 300 mm. Fig. 4.11 shows the excess current change for three different positions which are 43 cm away from the SLM, 42 cm away from the SLM and 41 cm away from the SLM. The closer GaAs to the lens, the larger the beam dimensions. In consequence, as the beam gets larger, more light is concentrated by the algorithm on the solar cell, which rises the current measured after the optimization and the excess current accordingly.

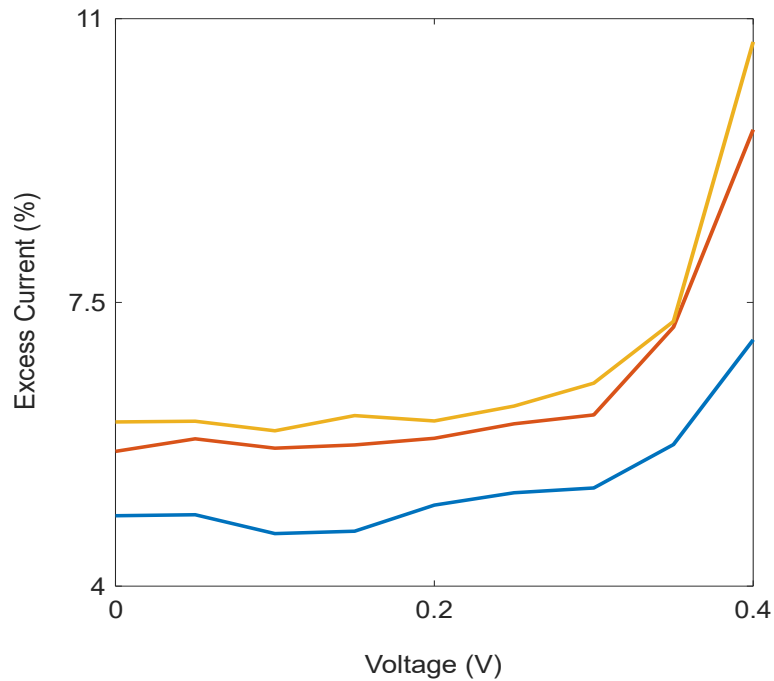


Figure 4.11: Calculated excess current for different positions. The current for blue curve is for when GaAs is placed 43 cm after SLM. The current for red curve is for when GaAs is placed 42 cm after SLM. The current for yellow curve is for when GaAs is placed 41 cm after SLM.

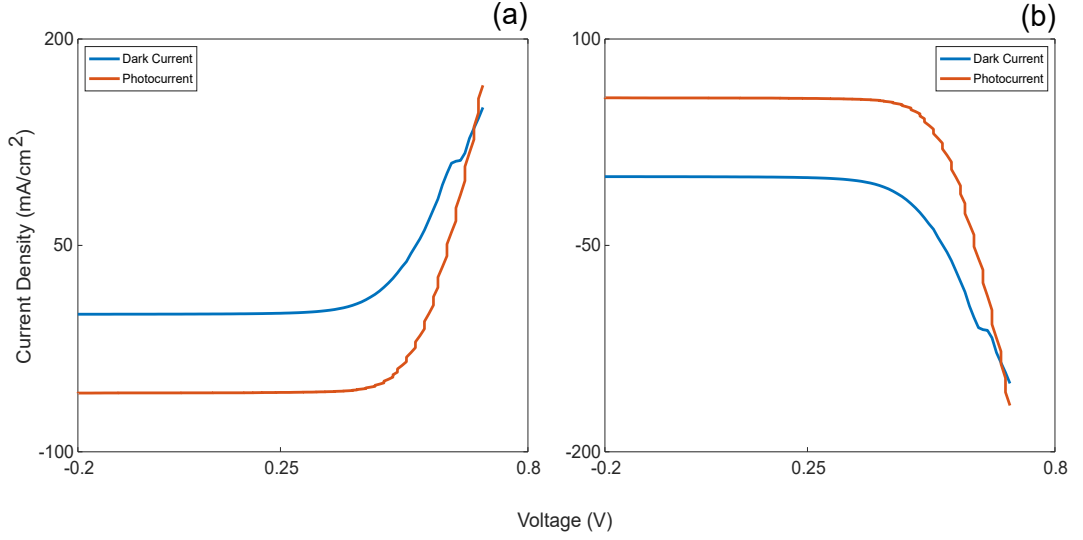


Figure 4.12: (a) The reference current for dark current and photocurrent of Si, and (b) the converted data to the first quadrant for convenience.

4.3 Optimization of Si Solar Cell via Wavefront Shaping

4.3.1 Reference and Noise Measurements of Si

Under 1 sun ($100 \text{ mW}/\text{cm}^2$) illumination, Si has an open circuit voltage of 579 mV. Without illumination, the open circuit voltage of the dark current is 12 mV. Fig. 4.12 shows the dark and photocurrent, while Fig. 4.12 corresponds to the same measurement, but the data is converted to the first quadrant for convenience.

The measurements of short circuit current, fill factor and efficiency are $\sim 19 \text{ mA}/\text{cm}^2$, 73% and 9%, respectively. The maximum power is measured as 24 mW, MPP voltage as $\sim 456 \text{ mV}$ and MPP current density as $\sim 18 \text{ mA}/\text{cm}^2$.

Fig. 4.13 shows the noise measurement for Si solar cell that is taken for three hours at each voltage value from 0 V to the open circuit voltage of 3 mV. The optimization voltage is chosen as 0 V where the noise is 1.3%. The measurement is taken with the setup in Fig. 3.1.

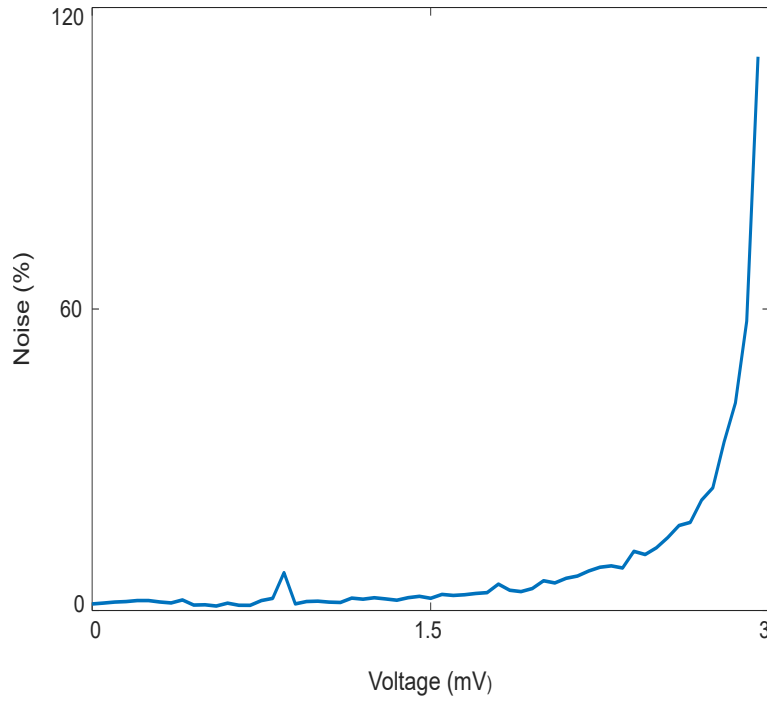


Figure 4.13: Si noise measurement is calculated according to the equation 43. The noise is below 10% until 2.4 mV bias.

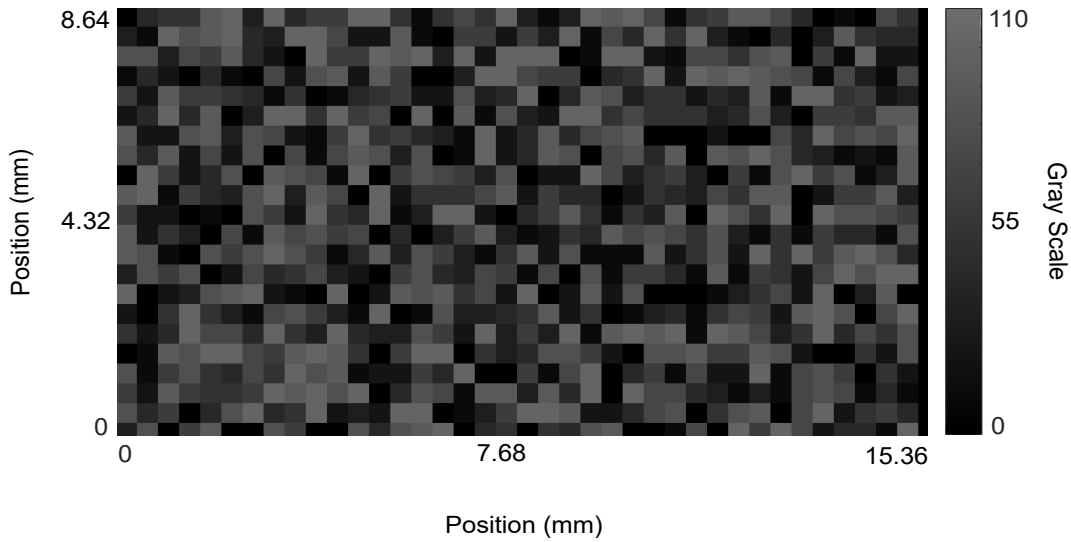


Figure 4.14: The optimized SLM phase pattern for Si solar cell by using the same algorithm for optimization of GaAs solar cell. It is evident that there is no concentration on the solar cell.

The phase pattern optimized for Si solar cell is Fig. 4.14. By observing the SLM

pattern, it can be concluded that there is no concentration on Si solar cell. Therefore, there is no excess current measured from Si which the measurement from Keithley also proves. We claim that the topography of Si solar cell affects the way of working of our algorithm. GaAs has a polished surface which boosts signals for the SLM while Si has a rough surface. Additionally, we have a very low power light source which is 10 mW. The optical elements on the optical path also reduce the power of incident light on solar cells to extremely low values that even conventional power sensor cannot measure. That is why, the power of the light source is not enough to force Si solar cell to operate. Another reason is that, Si solar cell has a lot of shading due to bus bars which decrease the intensity of the light solar cell receiving even more.

4.4 Enhancing Performance of the Silicon Photodetector

The concentration of broadband light on Si photodetector is performed on the setup 3.1.

4.4.1 Noise Measurement of the Si Photodetector

The noise measurement data for silicon photodetector is taken for three hours. It is calculated according to the equation 47, and below 1% which is 0.004%. The measurement is taken with the setup in Fig. 3.1.

$$\text{Noise (\%)} = 100 \times \frac{\text{Standard deviation of the RMS}}{\text{Mean value of the RMS}} \quad (47)$$

4.4.2 Achieving Excess Current via Concentration on the Si Photodetector

Fig. 4.15 shows the phase patterns which are obtained on the SLM surface for silicon photodetector. The photodetector is placed in the middle of the beam and the broadband light is concentrated on it. The structure of the photodetector is clearly seen on the phase pattern.

$$\text{Excess RMS Value (\%)} = 100 \times \frac{\text{RMS}_{\text{optimization}} - \text{RMS}_{\text{light}}}{\text{RMS}_{\text{light}} - \text{RMS}_{\text{dark}}} \quad (48)$$

$$\text{Excess RMS Value (\%)} = 100 \times \frac{\text{RMS}_{\text{optimization}} - \text{RMS}_{\text{light}}}{\text{RMS}_{\text{light}}} \quad (49)$$

RMS value is measured with an oscilloscope. The excess RMS value with dark current is found via the equation 48 as 6.13%, 9.5%, 10.6%, 12.3% and 9.8% for 20736 superpixels, 5184 superpixels, 2304 superpixels, 1296 superpixels and 829 superpixels, respectively. In the equation, $\text{RMS}_{\text{optimization}}$ is the RMS value measured when the SLM pattern is reflected on the silicon photodetector, $\text{RMS}_{\text{light}}$ is the RMS value measured when there is no phase pattern on the SLM and RMS_{dark} is the current when there is no illumination on the photodetector. Additionally, via equation 49, the excess RMS value is calculated without dark current as 6%, 9.2%, 10.3%, 12% and 9.5% for 20736 superpixels, 5184 superpixels, 2304 superpixels, 1296 superpixels and 829 superpixels, respectively.

Number of Superpixels	Excess RMS Value with Dark (%)	Excess RMS Value without Dark (%)
20736	6.13	6
5184	9.5	9.2
2304	10.6	10.3
1296	12.3	12
829	9.8	9.5

Table 4.4: The calculated excess RMS value of silicon photodetector for five different number of superpixels.

4.5 Enhancing Performance of the InGaAs Photodetector

The concentration of broadband light on InGaAs photodetector is performed on the setup 3.1.

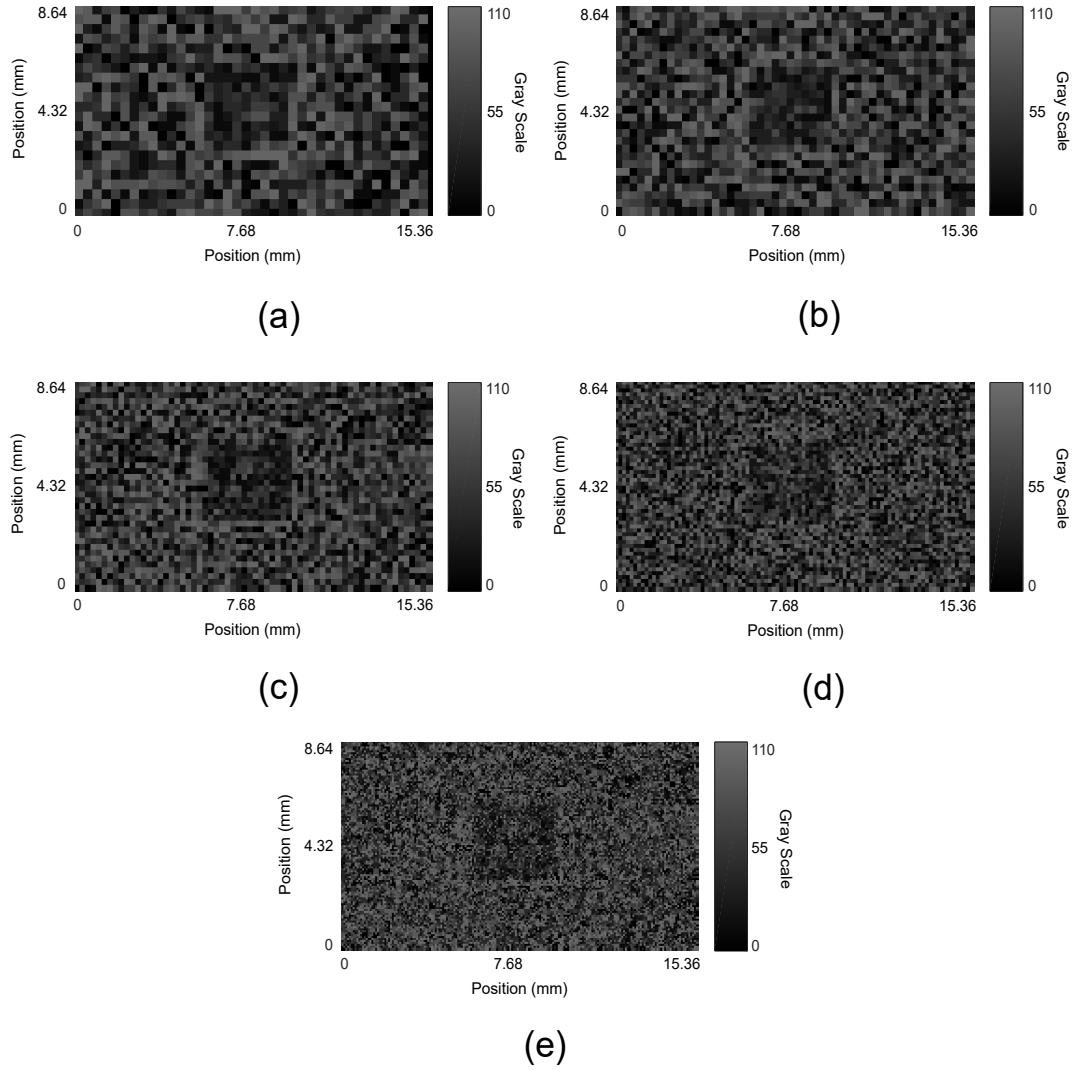


Figure 4.15: SLM phase pattern for silicon photodetector optimized with (a) 829 superpixels (b) 1296 superpixels (c) 2304 superpixels (d) 5184 superpixels (e) 20736 superpixels. The shape of silicon photodetector is clearly observed on the SLM phase pattern.

4.5.1 Noise Measurement of the InGaAs Photodetector

The noise measurement data for InGaAs photodetector is taken for three hours. It is calculated according to the equation 47, and found as 0.009%. The measurement is taken with the setup in Fig. 3.1.

4.5.2 Achieving Excess Current via Concentration on the InGaAs Photodetector

Fig. 4.16 shows the phase patterns which are obtained on the SLM surface for InGaAs photodetector. The photodetector is placed in the middle of the beam and the broadband light is concentrated on it. The structure of the photodetector is selected on the phase pattern.

RMS value is measured with an oscilloscope. The excess RMS value with dark current is found via the equation 48 as 9.8%, 12.63%, 16%, 15.52% and 16% for 20736 superpixels, 5184 superpixels, 2304 superpixels, 1296 superpixels and 829 superpixels, respectively. In addition to the calculations, via equation 49, the excess RMS value is calculated without dark current as 8.72%, 11%, 14%, 13.86% and 14% for 20736 superpixels, 5184 superpixels, 2304 superpixels, 1296 superpixels and 829 superpixels, respectively.

Number of Superpixels	Excess RMS Value with Dark (%)	Excess RMS Value without Dark (%)
20736	9.8	8.72
5184	12.63	11
2304	16	14
1296	15.52	13.86
829	16	14

Table 4.5: The calculated excess RMS value of InGaAs photodetector for five different number of superpixels.

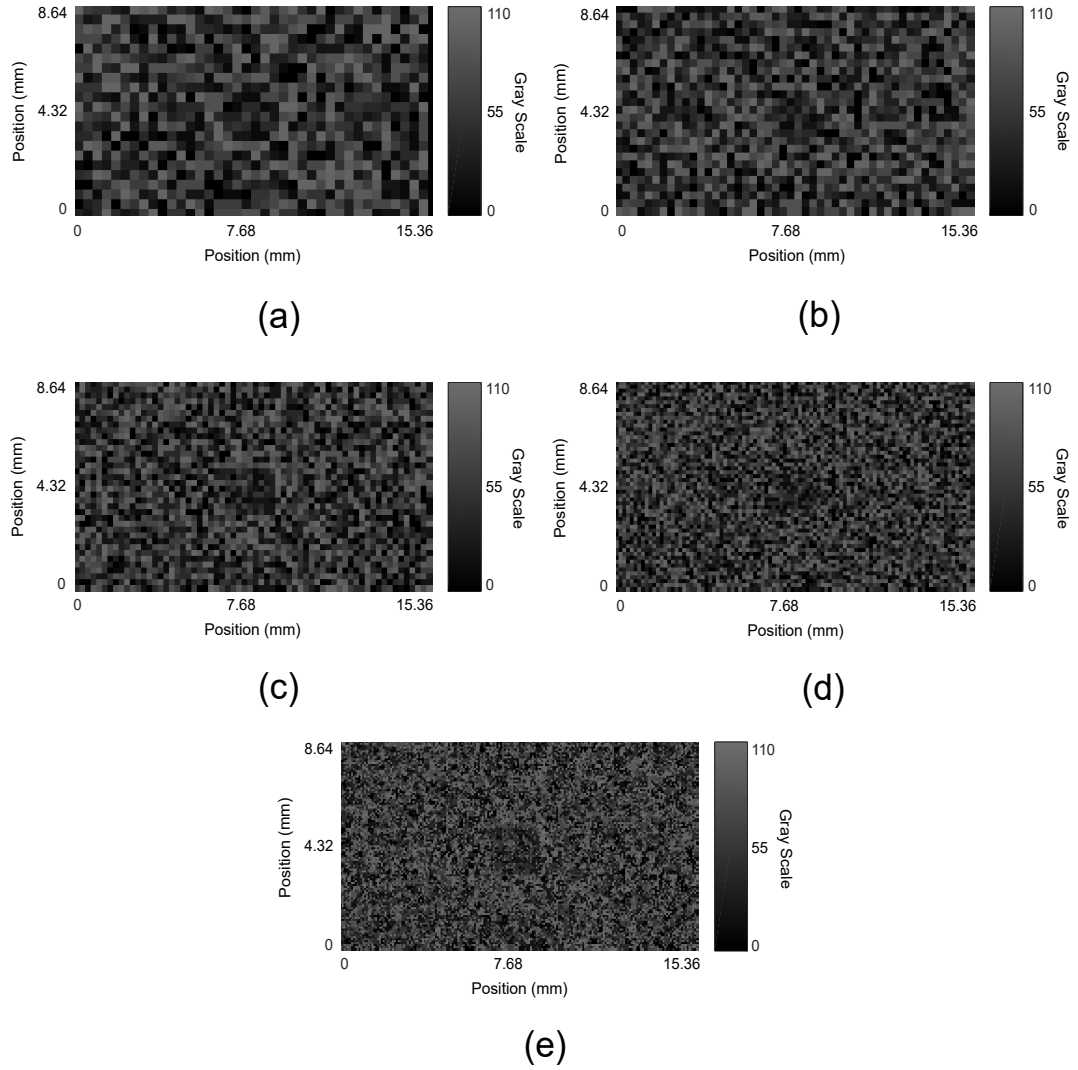


Figure 4.16: SLM phase pattern for InGaAs photodetector optimized with (a) 829 superpixels (b) 1296 superpixels (c) 2304 superpixels (d) 5184 superpixels (e) 20736 superpixels. The shape of InGaAs photodetector is clearly seen on the SLM phase pattern.

CHAPTER 5

CONCLUSION

In this study, we create a phase pattern on the surface of SLM in order to increase the performance of GaAs solar cell and Si/InGaAs photodetectors. The broadband light source is concentrated on the solar cell and photodiodes. As a result, we obtain the current, power and RMS voltage values measured from GaAs solar cell and Si/InGaAs photodetectors, respectively. We obtain an excess current up to $\sim 20\%$ from GaAs solar cell, an excess RMS voltage value up to $\sim 12\%$ from Si photodetector and an excess RMS voltage value up to $\sim 16\%$ from InGaAs photodetector. Open circuit voltage increase for GaAs solar cell is measured as ~ 5 mV which indicates that the concentration is achieved successfully on the solar cell.

Instead of conventional calculation and fabrication methods to obtain a DOE, we experimentally emulate a DOE via the SLM. In this way, the fabrication errors which cause a difference in the calculated results and experimental results are eliminated. Additionally, the phase pattern obtained on the surface of the SLM can be transformed into a physical DOE by converting encoded gray values on the SLM to the corresponding height values. Having an effortless fabrication process and compact size make the large-scale production to enhance the performance of solar cells attainable for the future of harvesting the solar energy. Our method can also be utilized for enhancing the efficiency of quantum sources and for increasing detection rates by spatial and spectral control of the excitation or emission signals.

REFERENCES

- [1] B. M. Kayes, H. Nie, R. Twist, S. G. Spruytte, F. Reinhardt, I. C. Kizilyalli, and G. S. Higashi, “27.6single-junction solar cells under 1 sun illumination,” *Conference Record of the IEEE Photovoltaic Specialists Conference*, pp. 000004–000008, 2011.
- [2] B. N. Gün and E. Yüce, “Wavefront shaping assisted design of spectral splitters and solar concentrators,” *Scientific Reports*, vol. 11, no. 1, pp. 1–7, 2021.
- [3] “Standard solar spectra.” <https://www.pveducation.org/pvcdrom/appendices/standard-solar-spectra>.
- [4] “Our technology.” <https://qdsolarinc.com/technology/>, 2020.
- [5] B. Saleh and M. Teich, *Fundamentals of Photonics*. John Wiley Sons Inc., 1991.
- [6] “Theory: Fresnel zone plate theory and equations. learn about zone locations, resolution, bandwidth restrictions, and field of view.” <http://zoneplate.lbl.gov/theory>, 2014.
- [7] C. Palmer, *Diffraction Grating Handbook*. MKS Instruments, Inc., 2020.
- [8] G. J. Swanson, “Binary Optics Technology : The Theory and Design of Multi-level Diffractive Optical Elements,” *Contract*, pp. 1–53, 1989.
- [9] Hamamatsu Photonics K.K., *Phase spatial light modulator LCOS-SLM*.
- [10] G. Thuillier, D. Labs, T. Foujols, W. Peetermans, D. Gillotay, P. C. Simon, and H. Mandel, “The solar spectral irradiance from 200 to 2400 nm as measured by the solspec spectrometer from the atlas and eureka missions,” *Solar Physics*, vol. 214, pp. 1–22, 2003.
- [11] E. H. Ciftpinar, “Selective emitter formation via single step doping through laser

patterned mask oxide layer for monocrystalline silicon solar cells,” September 2014.

- [12] P. Würfel and U. Würfel, *Physics of Solar Cells: From Basic Principles to Advanced Concepts*. Wiley-VCH, 2016.
- [13] C. Hu and R. M. White, *Solar cells: from basic to advanced systems*. McGraw-Hill Inc., 1983.
- [14] W. Shockley and H. J. Queisser, “Detailed balance limit of efficiency of p-n junction solar cells,” *Journal of Applied Physics*, vol. 32, no. 3, pp. 510–519, 1961.
- [15] M. A. Green, E. D. Dunlop, J. Hohl-Ebinger, M. Yoshita, N. Kopidakis, K. Bothe, D. Hinken, M. Rauer, and X. Hao, “Solar cell efficiency tables (Version 60),” *Progress in Photovoltaics: Research and Applications*, no. May, pp. 687–701, 2022.
- [16] Q. Huang, P. Qi, J. Hu, H. Xu, C. Jiang, and Q. Liu, “Design of a high-efficiency and low-cost reflection-type diffractive optical element as the spectrum splitting solar concentrator for lateral multi-junction solar cells architecture,” *Proceedings of 2016 IEEE Advanced Information Management, Communicates, Electronic and Automation Control Conference, IMCEC 2016*, pp. 1528–1532, 2017.
- [17] J. Z. Wang, Q. L. Huang, X. Xu, B. G. Quan, J. H. Luo, Y. Zhang, J. S. Ye, D. M. Li, Q. B. Meng, and G. Z. Yang, “Realizing high photovoltaic efficiency with parallel multijunction solar cells based on spectrum-splitting and -concentrating diffractive optical element,” *Chinese Physics B*, vol. 24, no. 5, 2015.
- [18] J. C. Goldschmidt, C. Do, M. Peters, and A. Goetzberger, “Spectral splitting module geometry that utilizes light trapping,” *Solar Energy Materials and Solar Cells*, vol. 108, pp. 57–64, 2013.
- [19] M. Nakamura, K. Tada, T. Kinoshita, T. Bessho, C. Nishiyama, I. Takenaka, Y. Kimoto, Y. Higashino, H. Sugimoto, and H. Segawa, “Perovskite/CIGS Spectral Splitting Double Junction Solar Cell with 28Efficiency,” *iScience*, vol. 23, no. 12, p. 101817, 2020.

- [20] “Characterization of a Si/InGaAs lateral beam splitting photovoltaic system,” *I2MTC 2017 - 2017 IEEE International Instrumentation and Measurement Technology Conference, Proceedings*, pp. 0–4, 2017.
- [21] J. S. Ye, J. Z. Wang, Q. L. Huang, B. Z. Dong, Y. Zhang, and G. Z. Yang, “A single diffractive optical element implementing spectrum-splitting and beam-concentration functions simultaneously with high diffraction efficiency,” *Chinese Physics B*, vol. 22, no. 3, 2013.
- [22] Q. Huang, J. Wang, B. Quan, Q. Zhang, D. Zhang, D. Li, Q. Meng, L. Pan, Y. Wang, and G. Yang, “Design and fabrication of a diffractive optical element as a spectrum-splitting solar concentrator for lateral multijunction solar cells,” *Applied Optics*, vol. 52, no. 11, pp. 2312–2319, 2013.
- [23] A. Yolalmaz and E. Yuce, “Designs of diffractive optical elements for solar energy harvesting,” *5th International Conference on Power Generation Systems and Renewable Energy Technologies, PGSRET 2019*, no. 118, pp. 26–27, 2019.
- [24] N. Mohammad, P. Wang, D. J. Friedman, and R. Menon, “Enhancing photovoltaic output power by 3-band spectrum-splitting and concentration using a diffractive micro-optic,” *Optics Express*, vol. 22, no. S6, p. A1519, 2014.
- [25] G. Kim, J. A. Dominguez-Caballero, H. Lee, D. J. Friedman, and R. Menon, “Increased photovoltaic power output via diffractive spectrum separation,” *Physical Review Letters*, vol. 110, no. 12, pp. 1–5, 2013.
- [26] R. Gerchberg and W. Saxton, “A practical algorithm for the determination of phase from image and diffraction plane pictures,” *Optik*, vol. 35, p. 237–250, 1972.
- [27] G.-z. Yang, B.-z. Dong, B.-y. Gu, J.-y. Zhuang, and O. K. Ersoy, “Gerchberg-Saxton and Yang-Gu algorithms,” vol. 33, no. 2, pp. 209–218, 1994.
- [28] M. A. Seldowitz, J. P. Allebach, and D. W. Sweeney, “Synthesis of digital holograms by direct binary search,” *Applied Optics*, vol. 26, no. 14, p. 2788, 1987.
- [29] G. Zhou, Y. Chen, Z. Wang, and H. Song, “Genetic local search algorithm for optimization design of diffractive optical elements,” *Applied Optics*, vol. 38, no. 20, p. 4281, 1999.

- [30] I. Mingareev, R. Berlich, T. J. Eichelkraut, H. Herfurth, S. Heinemann, and M. C. Richardson, “Diffractive optical elements utilized for efficiency enhancement of photovoltaic modules,” *Optics Express*, vol. 19, no. 12, p. 11397, 2011.
- [31] M. Skeren, I. Richter, and P. Fiala, “Iterative Fourier transform algorithm: different approaches to diffractive optical element design,” *Laser Beam Shaping III*, vol. 4770, no. October 2002, p. 75, 2002.
- [32] H. Kim and B. Lee, “Optimal design of diffractive optical elements with functional relationship between phase and amplitude modulations using nonlinear optimization methods,” *Laser Beam Shaping VI*, vol. 5876, no. August 2005, p. 587611, 2005.
- [33] W. Qu, H. Gu, Q. Tan, and G. Jin, “Precise design of two-dimensional diffractive optical elements for beam shaping,” *Applied Optics*, vol. 54, no. 21, p. 6521, 2015.
- [34] M. Kusko, D. Cojoc, D. Apostol, R. Muller, E. Manea, and C. Podaru, “Design and fabrication of diffractive optical elements,” *Proceedings of the International Semiconductor Conference, CAS*, vol. 1, no. June 2014, pp. 167–170, 2003.
- [35] J. Gary and J. Swanson, “in infrared systems Diffractive,” no. 6, pp. 605–608, 2015.
- [36] A. Yolalmaz and E. Yüce, “Spectral splitting and concentration of broadband light using neural networks,” *APL Photonics*, vol. 6, no. 4, 2021.
- [37] L. Wang, T. Tschudi, T. Halldórsson, and P. R. Pétursson, “Speckle reduction in laser projection systems by diffractive optical elements,” *Applied Optics*, vol. 37, no. 10, pp. 1770–1775, 1998.
- [38] G. J. Swanson, “Binary Optics Technology : Theoretical Limits on the Diffraction Efficiency of Multilevel Diffractive Optical Elements,” *Technical report, Massachusetts Insititute of Tech Lexington Lincoln Lab*, vol. 914, p. 29, 1991.
- [39] G.-N. Nguyen, *Modeling, design and fabrication of diffractive optical elements based on nanostructures operating beyond the scalar paraxial domain*. PhD thesis, Sous le sceau de l’Université européenne de Bretagne, February 5, 2015.

- [40] B. N. Gun, “Wavefront shaping assisted design and application of effective diffractive optical elements providing spectral splitting and solar concentration: Splicons,” September 2020.
- [41] Thorlabs, *Compact Stabilized Broadband Light Sources*, June 16, 2016.
- [42] J. Leach, G. Sinclair, P. Jordan, J. Courtial, M. J. Padgett, J. Cooper, and Z. J. Laczik, “3D manipulation of particles into crystal structures using holographic optical tweezers,” *Optics Express*, vol. 12, no. 1, p. 220, 2004.
- [43] E. Haellstig, J. Stigwall, M. Lindgren, and L. Sjöqvist, “Laser beam steering and tracking using a liquid crystal spatial light modulator,” *Laser Systems Technology*, vol. 5087, no. August 2003, p. 13, 2003.
- [44] E. Hällstig, J. Stigwall, T. Martin, L. Sjöqvist, and M. Lindgren, “Fringing fields in a liquid crystal spatial light modulator for beam steering,” *Journal of Modern Optics*, vol. 51, no. 8, pp. 1233–1247, 2004.
- [45] A. Mrquez, C. Iemmi, J. Campos, J. C. Escalera, and M. J. Yzuel, “Programmable apodizer to compensate chromatic aberration effects using a liquid crystal spatial light modulator,” *Optics Express*, vol. 13, no. 3, p. 716, 2005.
- [46] W. Yu, T. Konishi, T. Hamamoto, H. Toyota, T. Yotsuya, and Y. Ichioka, “Polarization-multiplexed diffractive optical elements fabricated by subwavelength structures,” *Applied Optics*, vol. 41, no. 1, p. 96, 2002.
- [47] C. Maurer, A. Jesacher, S. Bernet, and M. Ritsch-Marte, “What spatial light modulators can do for optical microscopy,” *Laser and Photonics Reviews*, vol. 5, no. 1, pp. 81–101, 2011.
- [48] “Kelvin (4-wire) resistance measurement.” <https://www.allaboutcircuits.com/textbook/direct-current/chpt-8/kelvin-resistance-measurement>, May 2013.
- [49] “4-wire kelvin testing.” <https://www.cirris.com/learning-center/testing-guidelines/special-topics/40-4-wire-kelvin-testing>, 2021.